



# **NAVAL POSTGRADUATE SCHOOL**

**MONTEREY, CALIFORNIA**

## **THESIS**

### **PHOTONIC ANALOG-TO-INFORMATION RECEIVER SIGNAL PROCESSING**

by

Daniel A. Blue

March 2019

Thesis Advisor:

Co-Advisor:

Phillip E. Pace

James Calusdian

**Approved for public release. Distribution is unlimited.**

THIS PAGE INTENTIONALLY LEFT BLANK

<b>REPORT DOCUMENTATION PAGE</b>			<i>Form Approved OMB No. 0704-0188</i>	
Public reporting burden for this collection of information is estimated to average 1 hour per response, including the time for reviewing instruction, searching existing data sources, gathering and maintaining the data needed, and completing and reviewing the collection of information. Send comments regarding this burden estimate or any other aspect of this collection of information, including suggestions for reducing this burden, to Washington headquarters Services, Directorate for Information Operations and Reports, 1215 Jefferson Davis Highway, Suite 1204, Arlington, VA 22202-4302, and to the Office of Management and Budget, Paperwork Reduction Project (0704-0188) Washington, DC 20503.				
<b>1. AGENCY USE ONLY (Leave blank)</b>	<b>2. REPORT DATE</b> March 2019	<b>3. REPORT TYPE AND DATES COVERED</b> Master's thesis		
<b>4. TITLE AND SUBTITLE</b> PHOTONIC ANALOG-TO-INFORMATION RECEIVER SIGNAL PROCESSING			<b>5. FUNDING NUMBERS</b>	
<b>6. AUTHOR(S)</b> Daniel A. Blue				
<b>7. PERFORMING ORGANIZATION NAME(S) AND ADDRESS(ES)</b> Naval Postgraduate School Monterey, CA 93943-5000			<b>8. PERFORMING ORGANIZATION REPORT NUMBER</b>	
<b>9. SPONSORING / MONITORING AGENCY NAME(S) AND ADDRESS(ES)</b> N/A			<b>10. SPONSORING / MONITORING AGENCY REPORT NUMBER</b>	
<b>11. SUPPLEMENTARY NOTES</b> The views expressed in this thesis are those of the author and do not reflect the official policy or position of the Department of Defense or the U.S. Government.				
<b>12a. DISTRIBUTION / AVAILABILITY STATEMENT</b> Approved for public release. Distribution is unlimited.			<b>12b. DISTRIBUTION CODE</b> A	
<b>13. ABSTRACT (maximum 200 words)</b> <p>Modern electronic warfare systems require increasingly larger bandwidth monitoring ability. Analog-to-information techniques increase bandwidth-monitoring capability without increasing the performance requirements placed on analog-to-digital converters. Two analog-to-information compressive sensing receiving methodologies capable of recovering signal information below the Nyquist sampling rate are considered. The designing and simulation of these receiving methodologies using photonic components in MATLAB and OptSim shows successful information recovery below the Nyquist rate. Finally, prototype receiver models were implemented using commercial off-the-shelf equipment, demonstrating rudimentary capability of recovering compressed radio frequency signal information using Mach-Zehnder interferometers as sampling devices.</p>				
<b>14. SUBJECT TERMS</b> compressed sensing, electronic warfare, photonics			<b>15. NUMBER OF PAGES</b> 89	
			<b>16. PRICE CODE</b>	
<b>17. SECURITY CLASSIFICATION OF REPORT</b> Unclassified	<b>18. SECURITY CLASSIFICATION OF THIS PAGE</b> Unclassified	<b>19. SECURITY CLASSIFICATION OF ABSTRACT</b> Unclassified	<b>20. LIMITATION OF ABSTRACT</b> UU	

THIS PAGE INTENTIONALLY LEFT BLANK

**Approved for public release. Distribution is unlimited.**

**PHOTONIC ANALOG-TO-INFORMATION RECEIVER SIGNAL  
PROCESSING**

Daniel A. Blue  
Lieutenant, United States Navy  
BS, U.S. Naval Academy, 2010

Submitted in partial fulfillment of the  
requirements for the degree of

**MASTER OF SCIENCE IN ELECTRICAL ENGINEERING**

from the

**NAVAL POSTGRADUATE SCHOOL  
March 2019**

Approved by: Phillip E. Pace  
Advisor

James Calusdian  
Co-Advisor

Clark Robertson  
Chair, Department of Electrical and Computer Engineering

THIS PAGE INTENTIONALLY LEFT BLANK

## **ABSTRACT**

Modern electronic warfare systems require increasingly larger bandwidth monitoring ability. Analog-to-information techniques increase bandwidth-monitoring capability without increasing the performance requirements placed on analog-to-digital converters. Two analog-to-information compressive sensing receiving methodologies capable of recovering signal information below the Nyquist sampling rate are considered. The designing and simulation of these receiving methodologies using photonic components in MATLAB and OptSim shows successful information recovery below the Nyquist rate. Finally, prototype receiver models were implemented using commercial off-the-shelf equipment, demonstrating rudimentary capability of recovering compressed radio frequency signal information using Mach-Zehnder interferometers as sampling devices.

THIS PAGE INTENTIONALLY LEFT BLANK



# TABLE OF CONTENTS

<b>I.</b>	<b>INTRODUCTION.....</b>	<b>1</b>
<b>A.</b>	<b>MOTIVATION .....</b>	<b>1</b>
<b>B.</b>	<b>PREVIOUS WORK.....</b>	<b>2</b>
<b>C.</b>	<b>OBJECTIVE .....</b>	<b>2</b>
<b>D.</b>	<b>THESIS CHAPTER BREAKDOWN .....</b>	<b>2</b>
<b>II.</b>	<b>BACKGROUND .....</b>	<b>3</b>
<b>A.</b>	<b>NYQUIST RATE SAMPLING AND ALIASING .....</b>	<b>3</b>
<b>B.</b>	<b>ANALOG-TO-INFORMATION THEORY AND METHODS .....</b>	<b>4</b>
1.	Analog-To-Information Converters .....	5
2.	Compressive Sensing .....	5
3.	Compressive Sensing Information Recovery.....	7
4.	The Nyquist Folding Receiver.....	7
5.	Asynchronous Multi-Rate Sampling Receiver .....	12
<b>C.</b>	<b>PHOTONIC COMPONENTS USED IN RADAR.....</b>	<b>13</b>
1.	Laser Diodes and Photodiodes.....	14
2.	Mach-Zehnder Interferometer Modulator.....	14
<b>III.</b>	<b>MATLAB SIGNAL PROCESSING SIMULATIONS .....</b>	<b>17</b>
<b>A.</b>	<b>NYQUIST FOLDING RECEIVER SIMULATION .....</b>	<b>17</b>
1.	Zero-Bandwidth, Zero-Noise Single-Tone Information Recovery.....	17
2.	Zero-Bandwidth Noisy-Channel Single Tone Information Recovery.....	21
3.	Zero-Bandwidth, Zero-Noise Multiple-Tone Information Recovery.....	22
4.	Zero-Bandwidth, Noisy-Channel Multiple-Tone Information Recovery.....	24
5.	Non-Zero Bandwidth Information Recovery .....	26
<b>B.</b>	<b>ASYNCHRONOUS MULTI-RATE SAMPLING RECEIVER.....</b>	<b>29</b>
<b>IV.</b>	<b>OptSim HARDWARE SIMULATIONS.....</b>	<b>37</b>
<b>A.</b>	<b>SINGLE-SOURCE PHOTONIC NYFR.....</b>	<b>39</b>
<b>B.</b>	<b>PHOTONIC ASYNCHRONOUS MULTI-RATE SAMPLING RECEIVER .....</b>	<b>44</b>
<b>V.</b>	<b>PHOTONIC A-TO-I RECEIVER HARDWARE TESTS .....</b>	<b>49</b>

A.	LINEARIZED MODULATOR NYFR TESTS.....	50
B.	DUAL MODULATOR NYFR TESTS.....	53
C.	DUAL MODULATOR WITH AMPLIFIER NYFR TESTS .....	57
VI.	CONCLUSIONS AND RECOMMENDATIONS.....	63
A.	CONCLUSIONS .....	63
B.	FUTURE WORK.....	64
1.	Analyzing the Output in the Optical Domain .....	64
2.	Improve the Prototype Build .....	64
	LIST OF REFERENCES.....	67
	INITIAL DISTRIBUTION LIST .....	69

## LIST OF FIGURES

Figure 1.	Comparison of a Signal Sampled at and Below the Nyquist Rate.....	4
Figure 2.	Representation of Compressive Sensing Model. Adapted from [11]. .....	6
Figure 3.	Nyquist Folding A-to-I Receiver Architecture. Adapted from [3]. .....	8
Figure 4.	Time and Frequency Domain of Frequency Modulated Pulse .....	9
Figure 5.	Nyquist Zones and Modulation Scale Factors. Adapted from [3]. .....	10
Figure 6.	NYFR Compressive Sensing Model. Source: [4]. .....	11
Figure 7.	Asynchronous Multi-Rate Sampling Receiver. Adapted from [6]. .....	12
Figure 8.	Mach-Zehnder Interferometer.....	15
Figure 9.	Mach-Zehnder Interferometer Transfer Characteristic Graph. Adapted from [13].....	16
Figure 10.	NYFR MATLAB Simulation Block Diagram.....	17
Figure 11.	Sample Clock Modulation .....	18
Figure 12.	Frequency Spectrogram of Undersampled Signal $f_I = 1.15$ GHz .....	19
Figure 13.	SPGL1 Algorithm Spectrum Recovery of 1.15-GHz Undersampled Signal .....	20
Figure 14.	Frequency Spectrum of Noisy Undersampled Signal $f_I = 1.15$ GHz .....	21
Figure 15.	SPGL1 Algorithm Spectrum Recovery of 1.15-GHz Noisy Undersampled Signal. ....	22
Figure 16.	Frequency Spectrogram of NYFR Output for Signal Tones in Table 2.....	23
Figure 17.	SPGL1 Algorithm Spectrum Recovery of NYFR Output for Signal Tones in Table 2.....	24
Figure 18.	Nyquist Rate Sampled Spectrogram for Table 2 Signals with Noise .....	25
Figure 19.	Undersampled Spectrogram for Table 2 Signals with Noise.....	25
Figure 20.	SPGL1 Spectrum Recovery for Table 2 Signals with Noise .....	26

Figure 21.	Nyquist Rate and NYFR Frequency Spectrum of Simulation #1 from Table 3. ....	27
Figure 22.	Nyquist Rate and NYFR Frequency Spectrum of Simulation #2 from Table 3. ....	28
Figure 23.	Nyquist Rate and NYFR Frequency Spectrum of Simulation #3 from Table 3. ....	28
Figure 24.	Asynchronous Multi-Rate Sampling Receiver MATLAB Block Diagram.....	29
Figure 25.	Original Signal with Corresponding Undersampling Points .....	30
Figure 26.	Undersampled Channel Frequency Spectrum.....	31
Figure 27.	Sampling Channel Aliasing Spectra .....	32
Figure 28.	Sampling Channel 1 Aliasing Spectra .....	33
Figure 29.	Sampling Channel 4 Aliasing Spectra .....	33
Figure 30.	(a) Nyquist Rate Spectrum Sample (b) Sampling Channel 3 Aliasing Spectra.....	34
Figure 31.	1.33-GHz BW: 40 MHz (a) Nyquist Rate Spectrum Sample (b) Aliasing Spectra .....	35
Figure 32.	2.6-GHz BW: 40 MHz(a) Nyquist Rate Spectrum Sample (b) Aliasing Spectra .....	35
Figure 33.	3.76-GHz BW: 40MHz (a) Nyquist Rate Spectrum Sample (b) Aliasing Spectra .....	35
Figure 34.	OptSim Model of Single-Source Photonic NYFR.....	39
Figure 35.	OptSim Pulses at Output of MZI .....	40
Figure 36.	Linear Amplitude MZI Transfer Characteristic Graph. Adapted from [13]......	41
Figure 37.	OptSim Simulation SPGL1 Recovery .....	42
Figure 38.	OptSim Simulation SPGL1 Recovery with Noise Added .....	43
Figure 39.	OptSim Simulation SPGL1 Recovery with Noise and Filtered Bias.....	43
Figure 40.	OptSim Model of Multiple Rate Receiver .....	44

Figure 41.	OptSim Multi-Rate Receiver Sampling Channel 1 Results .....	45
Figure 42.	OptSim Multi-Rate Receiver Sampling Pulse Shape.....	46
Figure 43.	OptSim Multi-Rate Receiver Aliasing Spectra.....	47
Figure 44.	JDSU Optical Linearized Modulator .....	50
Figure 45.	Optical Linearized Modulator Laboratory Setup.....	51
Figure 46.	Optical Linearized Modulator Pulse .....	52
Figure 47.	Optical Linearized Photonic NYFR Output.....	53
Figure 48.	Dual Modulator Laboratory Setup .....	54
Figure 49.	Dual Modulator Optical Pulses .....	55
Figure 50.	Dual Modulator Undersampling .....	55
Figure 51.	Photonic NYFR Spectrogram .....	57
Figure 52.	Photonic NYFR Normalized Frequency Response.....	57
Figure 53.	Dual Modulator with Amplifier Laboratory Setup .....	58
Figure 54.	Photonic NYFR with Amplifier Pulse Train .....	59
Figure 55.	Photonic NYFR with Amplifier Nyquist Rate Results .....	59
Figure 56.	Photonic NYFR with Amplifier Undersampled Results #1.....	60
Figure 57.	Photonic NYFR with Amplifier Undersampled Results #2.....	61

THIS PAGE INTENTIONALLY LEFT BLANK

## LIST OF TABLES

Table 1.	NYFR MATLAB Simulation Single Tone Recovery.....	18
Table 2.	NYFR MATLAB Simulation for Multiple Tones .....	23
Table 3.	NYFR Simulation with Bandwidth Signals Parameters .....	26
Table 4.	Asynchronous Multi-Rate Receiver Simulation Parameters .....	30
Table 5.	OptSim Hardware Model Description. Source: [13]. .....	37
Table 6.	Single Source Photonic NYFR Simulation Parameters .....	41
Table 7.	OptSim Multi-Rate Receiver Simulation Parameters .....	45
Table 8.	Laboratory Test Equipment .....	49
Table 9.	Laboratory Test Sampling Pulse.....	56

THIS PAGE INTENTIONALLY LEFT BLANK



## LIST OF ACRONYMS AND ABBREVIATIONS

AIC	analog-to-information converter
A-to-I	analog-to-information
ADC	analog-to-digital converter
AWGN	additive white Gaussian noise
BP	basic pursuit
BPDN	basic pursuit denoise
CPU	central processing unit
CS	compressive sensing
CWC	Cryptologic Warfare Community
DFT	discrete Fourier transform
EW	electronic warfare
FCC	Federal Communications Commission
FPGA	field-programmable gate array
MZI	Mach-Zehnder interferometer
NYFR	Nyquist Folding Receiver
RF	radio frequency
RADAR	radio detection and ranging
RIP	restricted isometry property
SIGINT	signals intelligence

THIS PAGE INTENTIONALLY LEFT BLANK

## **ACKNOWLEDGMENTS**

To the women in my life, LaTonya, Barbara, and Ethel; to Dr. James Calusdian; and to the American taxpayer. Thank you for your support.

THIS PAGE INTENTIONALLY LEFT BLANK

# **I. INTRODUCTION**

## **A. MOTIVATION**

The United States Navy's Cryptologic Warfare Community (CWC) is charged with conducting offensive and defensive cyber, electronic warfare (EW), and signals intelligence (SIGINT) operations both at sea and on land. A key aspect of accomplishing this mission is maintaining situational awareness of the radio frequency (RF) portion of the electromagnetic spectrum. Monitoring wide swaths of the RF spectrum allows the user to conduct signal environment mapping to detect and localize signals of interest and perform early warning operations in radar equipment to aid in the identification of adversary forces and the warning of threat radar.

Communication and radar technologies have increased rapidly since their inception due to the increasing capability of processing power, communication techniques, and manufacturing processes. As a result of these increases, the cost for entrance to exploit these technologies has decreased, causing the use of the available RF spectrum to increase. The average monthly mobile data traffic is projected to reach 49 exabytes by 2021. This is an increase of 680% from the 7.2 exabytes transmitted per month in 2016 [1]. This new data is transmitted using wideband and high frequency technologies, such as 5th Generation mobile communications and cognitive radios. The Federal Communications Commission (FCC) completed bidding on the 28GHz Upper Microwave Flexible Use Service licenses in January 2019; it auctioned off 2,695 licenses at a total cost of \$702,572,410 [2]. In addition to the increasing capability of communications technology, threat radar and weapons technology have also increased. Peer, near peer, and even hostile non-state adversaries have access to weapons and equipment that utilize frequencies at or greater than the X-band (8-12 GHz). An example of the threat this technological availability can pose to the Naval force is the recent launch of anti-ship cruise missiles at the USS RAMAGE off the Yemen coast by Houthi rebels.

As the entry point of communication and radar technology decreases and capability increases, the Navy will have to monitor an increasingly wider portion of the RF spectrum.

This requires the development of novel receiver architectures and processing algorithms to facilitate the monitoring of an ever-increasing number of signals within the RF spectrum. In addition, imperative to this mission is the need to accomplish the task in an efficient and cost effective manner.

## **B. PREVIOUS WORK**

In [3] and [4], the authors describe a Nyquist Folding Receiver (NYFR) capable of recovering signal information using a frequency-modulated, pulse-sampling technique at a rate significantly lower than the Nyquist Rate. In [5], Shmel designs, prototypes, and builds a single-source photonics-based NYFR and recovers signal information using time-frequency analysis techniques. In [6], Tzou et al. describe a low-cost multiband signal characterization technique to recover signal information at a lower-than-Nyquist rate.

## **C. OBJECTIVE**

In this thesis, the objective is to implement compressive sensing analog-to-information (A-to-I) techniques using photonic components in order to recover signal information using a lower-than-Nyquist sampling rate. Exploration of two compressive sensing models in MATLAB, their photonic based representations in OptSim, and experimental work conducted in the Optical Electronics Laboratory are used to assess the performance capability of photonic-based A-to-I receivers.

## **D. THESIS CHAPTER BREAKDOWN**

In this thesis, the theory of compressive sensing, the benefit of photonics in sensing technologies, the simulation of compressed sensing methodologies, and the implementation of compressed sensing methods using photonic components are discussed. The background information for the various methods and techniques used in this research is presented in Chapter II. The MATLAB simulation of the compressive sensing methods used in this research is presented in Chapter III. The hardware modeling and simulation for the photonics-based compressive sensing receivers is presented in Chapter IV. The implementation of two prototype receivers is presented in Chapter V. Lastly, conclusions, recommendations, and opportunities are presented for future research in Chapter VI.

## II. BACKGROUND

In this chapter the traditional method of sampling at the Nyquist rate and its limitations, recent developments of sampling at the information rate instead of the Nyquist rate, and two undersampling receiving methods are explored. Finally, a brief description of the benefits of photonics in radar and sensing systems and the components used in this research are reviewed.

### A. NYQUIST RATE SAMPLING AND ALIASING

The Nyquist-Shannon sampling theorem states that a band-limited continuous time signal  $x(t)$  with maximum frequency  $f_m$  can be completely recreated if equi-distant points are acquired with sampling interval  $T_s = 1/2f_m$ . The Nyquist-rate for sampling communication signals is  $f_s = 2 \cdot f_m$  [7]. The sampled waveform  $x_s[t]$  can be described using the unit impulse function

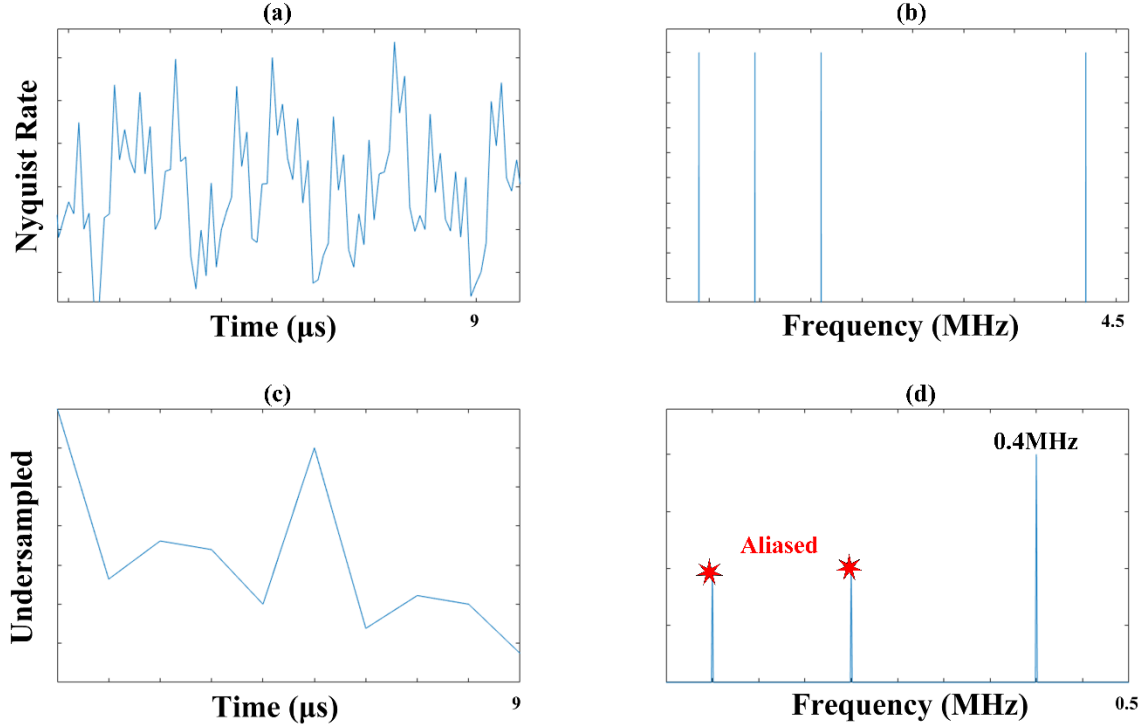
$$x_s[t] = \sum_{n=-\infty}^{+\infty} x[nT_s] \cdot \delta(t - nT_s). \quad (1)$$

The frequency domain of the sampled signal is defined by [8]

$$X_s(f) = \frac{1}{T_s} \sum_{k=-\infty}^{+\infty} X(f - f_s). \quad (2)$$

If the sampling frequency is set at less than twice the maximum frequency of the original signal, scaled duplicates of the signal appear at lower frequencies in the spectrum of  $x_s[t]$ ; this is known as aliasing. A Nyquist rate sample for a signal with four frequency tones at 0.4 MHz, 0.95 MHz, 1.6 MHz, and 4.2 MHz are compared to the same signal sampled at a rate of 1 MS/s; the results are shown in Figure 1. As seen in Figure 1b, when the original signal is sampled at the appropriate sampling frequency of 8.4 MS/s or greater, then  $X_s(f)$  displays the original frequency tones correctly. In Figure 1d, the signal was sampled at  $f_s = 1$  MS/s and does not contain all of the correct frequency tones. A sample

rate of 1 MS/s is greater than the Nyquist rate for the 0.4 MHz tone, so it is able to correctly recover this tone's frequency information; however, all of the other frequency tones are aliased and incorrectly identified in  $X_s(f)$ .



(a) Nyquist Rate Time-Domain Sample (b) Nyquist Rate Frequency-Domain Recovery (c) Below the Nyquist Rate Time Domain (d) Below the Nyquist Rate Frequency-Domain Recovery

Figure 1. Comparison of a Signal Sampled at and Below the Nyquist Rate

## B. ANALOG-TO-INFORMATION THEORY AND METHODS

In [9], Healy describes a new method of recovering information at the information rate instead of the Nyquist, or signal, rate. Fundamental to this method of information recovery is to compress the signal at the physical interface. New hardware with the ability to compress the information at the physical interface used in concert with current ADC technology is required.



## **1. Analog-To-Information Converters**

Many wideband receivers use Analog-to-Digital Converters (ADC) to process information. The ADCs must sample at the Nyquist rate to recover complete signal information and alleviate aliasing. As an example, consider a naval ship tasked with monitoring a 1 GHz sector of the RF spectrum for an unknown signal. The ADC must sample at a rate of 2 GS/s to recover all signal information; if a resolution of 12 bits was required, the ADC would have a maximum allowable aperture jitter, the sample-to-sample variation, of 0.0194 ps [10], which would be very difficult to achieve with today's technology. In addition to this requirement, the ADC must also limit sources of noise and nonlinearities, which increase as the sampling rate increases [9].

As the required range of wideband frequency monitoring increases, the performance required of ADCs also increases. Unlike conventional Central Processing Unit (CPU) development in which processing power doubles ever year, ADCs have been found to double in performance every two to four years [7]. Because of the limitations of ADCs, there has been a great interest in developing alternative methods of recovering information from the signal environment. Now consider a naval ship tasked with monitoring the same 1 GHz sector of the RF spectrum with prior knowledge of the signal environment or signal to be found. Utilizing information about this signal or the environment could potentially decrease the requirements placed on the ADC. In [9], Healy describes the objective of A-to-I Converters (AIC); unlike ADCs that only exploit one aspect of the signal, its maximum frequency, the goal of the AIC is to utilize prior knowledge of the signal environment or sampling method in concert with compressive techniques and algorithms to recover the signal using a maximum efficient sampling rate. The aim is to place an emphasis on the processing power provided by the CPU over performance of the ADC.

## **2. Compressive Sensing**

A fundamental requirement to applying compressive sensing techniques to an AIC is the assumption that the signal environment to be sampled is sparse. In this thesis, signals are referred to as being sparse in the Fourier, or frequency, domain. A signal is said to be

$k$ -sparse if a basis  $\Psi$  produces coefficients  $\alpha$  of mostly zero [11]. In reference to the A-to-I receiver, a signal in the time domain is considered to be sparse if most of the Fourier coefficients are zero [11]. The previous example of a naval ship searching for one signal in a 1 GHz portion of the spectrum would be considered sparse. A signal is defined as  $k$ -sparse if it has at most  $k$  non-zero values.

If a vector  $x$  with length  $N$  is sparse, then compressive sensing theory states that it can be sampled at a rate much lower than the Nyquist rate. A sampling matrix  $\Phi$  with dimensions  $M \times N$  can be applied to  $x$  to produce a compressed output vector  $y$  of length  $M$ , such that  $y = \Phi \cdot x$  where  $x = \Psi \cdot \alpha$ . The sensing matrix in this compressive sensing problem is defined as  $S = \Phi \cdot \Psi$ , such that  $y = S \cdot \alpha$ . A visual representation of the compressive sensing methodology of a  $k$ -sparse vector  $x$  of length  $N$  is shown in Figure 2 [11]. The sampling matrix must be wider than it is tall to ensure that there are more knowns than observations.

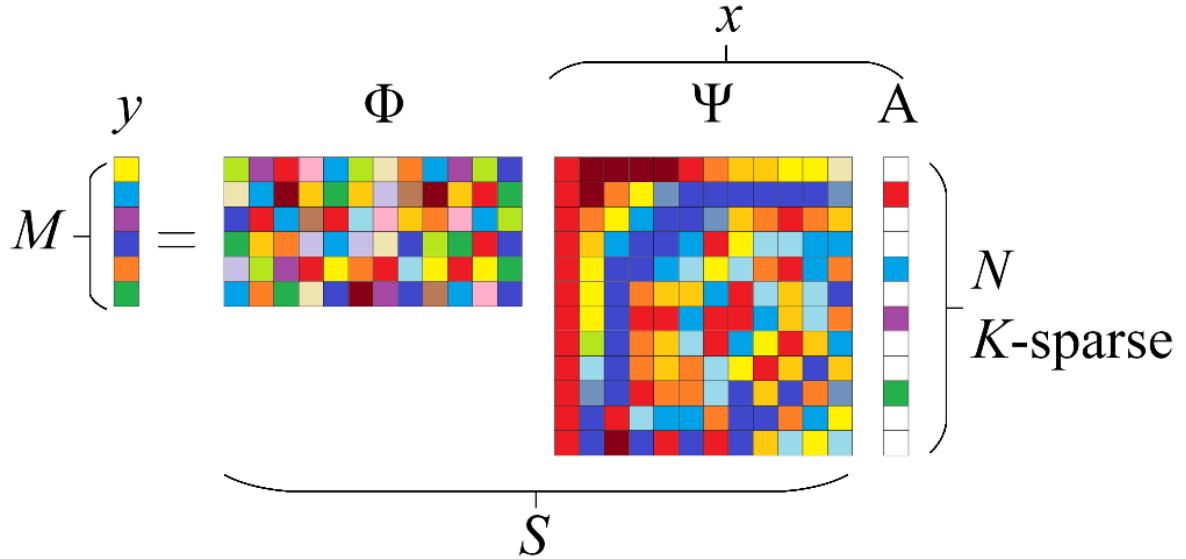


Figure 2. Representation of Compressive Sensing Model.  
Adapted from [11].

In order for compressive sensing to be utilized, four properties must be followed: 1) the basis must be orthonormal and its sensing matrix  $S$  must obey the 2) null space property, 3) it must adhere to the restricted isometry property (RIP), and 4) it must have a lower bound for coherence [11]. A matrix is orthonormal if its transpose is also its inverse, such that  $\Psi \cdot \Psi^T = I$ , where  $I$  is the identity matrix. The null space property states that the null space in a matrix should not be concentrated in a small set of indices [11]. The RIP ensures sparse reconstruction in the presence of error or noise. The RIP is defined by the following definition: the  $s$ th restricted isometry constant  $\delta_s = \delta_s(A)$  of a  $M \times N$  matrix  $A$  is the smallest  $\delta \geq 0$  such that

$$(1 - \delta)\|x\|_2^2 \leq \|Ax\|_2^2 \leq (1 + \delta)\|x\|_2^2, \quad (3)$$

for all  $s$ -sparse vectors of a  $1 \times N$  vector  $x$ . The matrix  $A$  is said to satisfy the RIP if  $\delta_s$  is small for a reasonably large  $s$  [11].

### 3. Compressive Sensing Information Recovery

The compressed vector  $y$  can be recovered after being undersampled by using a compressive sensing recovery algorithm. There are several types of compressive sensing (CS) recovery algorithms, but in this thesis we utilize the convex-optimization method for one-dimensional signals. A convex recovery algorithm minimizes a convex function for a sparse vector. A function is convex if a line between two points on the function lie above the function. The algorithm seeks to solve  $\min_x \{\|x\|_1 \text{ given } y = S \cdot x\}$  iteratively.

### 4. The Nyquist Folding Receiver

The initial receiver design used in this thesis was described by Fudge in 2008 and named the Nyquist Folding Receiver [3]. The NYFR is an A-to-I compression based receiver that utilizes an induced sample modulation to impart recoverable frequency information in the Fourier domain for narrowband signals. When a signal is undersampled, inaccurate (aliased) frequency results appear in a lower frequency band due to aliasing. If the NYFR uses a sampling rate with a wider bandwidth than the original signal's frequency,

the information is recoverable at the Nyquist-rate for the sample clock. A block diagram for the NYFR is shown in Figure 3.

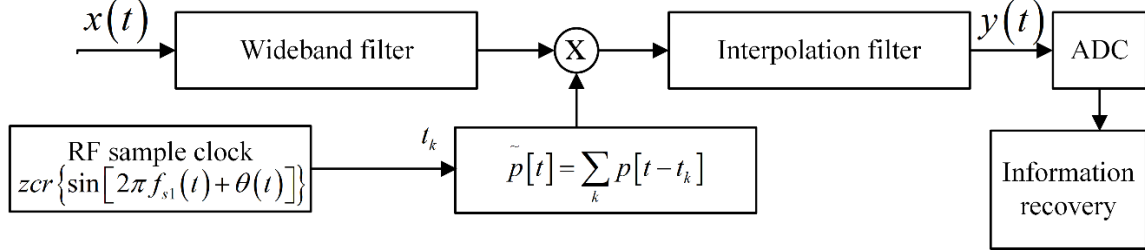
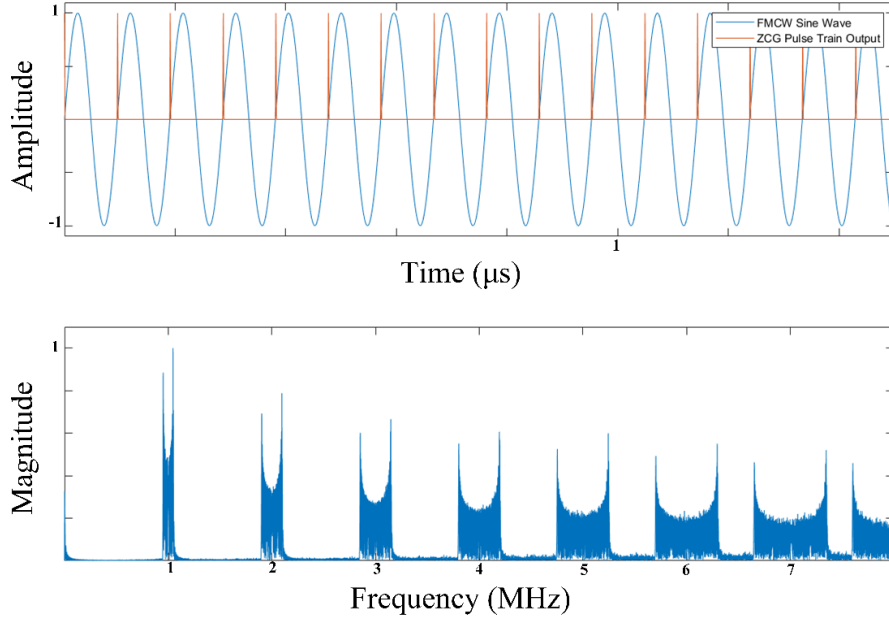


Figure 3. Nyquist Folding A-to-I Receiver Architecture.  
Adapted from [3].

The NYFR consists of a wideband preselect filter, a pulse train  $\tilde{p}[t]$  generated by a phase modulated sample clock, an interpolation filter, and an ADC. The sample clock is variable and is created by signaling a pulse on either the positive or negative zero crossings of a frequency modulated sine wave. The values that must be selected to create the sample clock are the center frequency  $f_{s1}$ , frequency sweep bandwidth  $f_{BW}$ , and frequency of the required sweep time  $f_{ST}$ . The phase modulation  $\theta(t)$  of the sample clock is

$$\theta(t) = \frac{f_{BW}}{f_{ST}} \sin(2\pi f_{ST} t). \quad (4)$$

A time and frequency domain representation of the sample clock and its corresponding pulse train  $\tilde{p}[t]$  is shown in Figure 4 for a center frequency of 1 MHz, a sweep bandwidth of 100 kHz, and a sweep time of 2.5 ms.



The pulse train output and its corresponding frequency response are shown. As the pulse train is represented in higher frequency harmonics, its width becomes greater.

Figure 4. Time and Frequency Domain of Frequency Modulated Pulse

The cut off of the interpolation filter is set to one-half of the average frequency of the sampling clock. The interpolation filter allows the output of the NYFR to be sampled at an ADC rate independent of the phase modulation of the input pulse train [3]. The output of the interpolation filter can be estimated as

$$y[t] \approx \sin \left[ 2\pi (f_I - f_{s1} \cdot k_H) t + \beta \psi[t] - M\theta[t] \right], \quad (5)$$

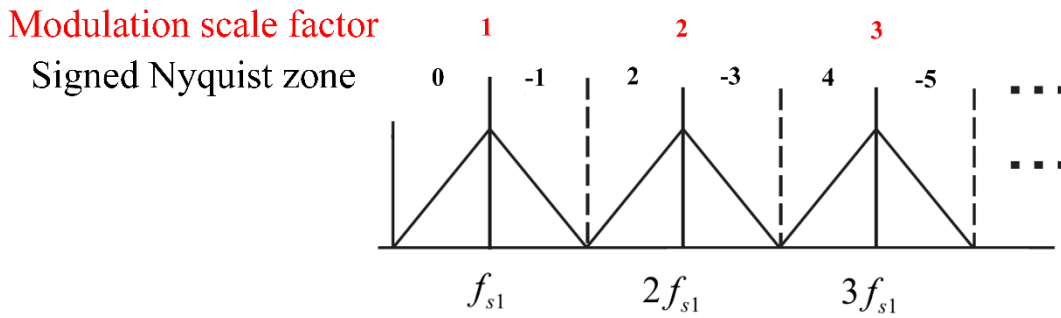
where  $f_I$  is the input frequency,

$$k_H = \text{round} \left( \frac{f_I}{f_{s1}} \right) \quad (6)$$

is the corresponding harmonic of the input frequency to the pulse train,

$$\beta = \text{sgn} \left[ 2\pi (f_I - f_{s1} k_H) \right] \quad (7)$$

dictates whether the output is a spectral reversal, and  $M = \beta \cdot k_H$  is the modulation scale factor [3]. In [3], Fudge also defines Nyquist zones; each harmonic of the pulse train has a positive and negative aspect that dictates whether the input signal is spectrally reversed. The Nyquist zones were defined to represent both the spectral property and the scale factor from which the input signal originated. The location of both the Nyquist zones and their corresponding modulation scale factors for a pulse train with center frequency  $f_{s1}$  is shown in Figure 5.



Modulation scale factors shown in red and signed Nyquist zones shown in black.

Figure 5. Nyquist Zones and Modulation Scale Factors. Adapted from [3].

In [4], a practical demonstration of the NYFR shows that signal information can be recovered via compressive sensing methods and develops a sensing matrix that adheres to the RIP ensuring convex optimization methods are able to recover the original frequency information of the input signal. An appealing aspect of the NYFR is that frequency recovery can be obtained by visual methods in addition to compressed sensing methods [4]. The NYFR compressive sensing model developed by Maleh in [4] is shown in Figure 6.

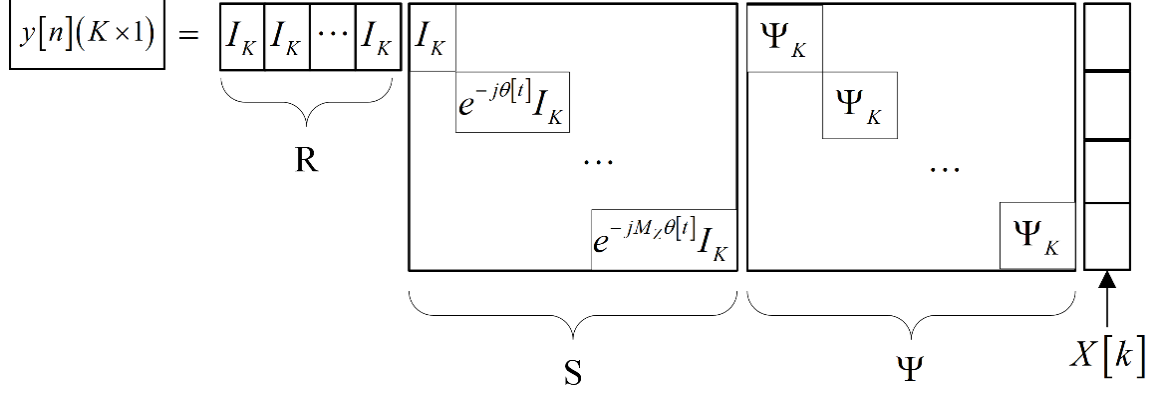


Figure 6. NYFR Compressive Sensing Model. Source: [4].

In Figure 6, the undersampled output vector of length  $K$  is represented by  $y[n]$ . The Nyquist-rate sampled input signal  $x[t]$  of length  $N$  can be represented by its Discrete Fourier Transform (DFT)  $X[k]$ . In order for the NYFR to properly function, the input signal must be sparse in the Fourier domain. The values for  $R$ ,  $S$ , and  $\Psi$  can be calculated given the modulating function of the sample pulse and the length of the compressed vector  $y[n]$ . In [4], Maleh presents this as a compressive sensing problem where  $y[n] = \Phi \cdot X[k]$  and can be solved using a convex recovery algorithm. The sensing matrix  $\Phi$  is equal to  $RS\Psi$  where  $R$  is the horizontal concatenation of  $Z$  identity matrices size  $K \times K$ ,  $S$  is the diagonal matrix of induced modulation by the sampling wave form size  $N \times N$ , and  $\Psi$  is the modified inverse discrete transform matrix of size  $N \times N$  given by [4]

$$\Psi = I_Z \otimes \Psi_K, \quad (8)$$

where  $\otimes$  is the Kronecker product.

A  $Z$ -dimension identity matrix is represented by  $I_Z$ , and  $\Psi_K$  is the inverse DFT matrix of size  $K$  in [4]. Computing the sensing matrix can be computationally difficult but reduces the requirements of the ADC. To compute the sensing matrix  $\Phi$  for a receiver monitoring 12 Nyquist zones, average sampling frequency of 1 GHz, modulation sweep time of 5  $\mu$ s, and an input signal of 4 GHz, the matrices required for sensing can encompass more than one billion data points.

## 5. Asynchronous Multi-Rate Sampling Receiver

The NYFR pulse train modulation induces a bandwidth onto the undersampled signal. As a result of this pulse train, signals with tones of larger bandwidth encounter reconstruction errors.

In [6], Tzou proposes a low-cost, multi-rate receiver that operates asynchronously, not requiring phase synchronization to recover sparse signals below the Nyquist rate. A stated benefit of the multi-rate receiver is that it does not mix wideband input signals with a multi-tone sampling signal that resonates spectral components across the monitored bandwidth, reducing and degrading reconstruction [6].

The multi-rate receiver is based on the concept of sampling a signal with two or more ADC channels operating below the Nyquist rate. It acquires information about the signal in two steps: it detects active input frequency bands at a low frequency resolution and characterizes the spectra of the active bands at a high frequency resolution. The receiver model is shown in Figure 7.

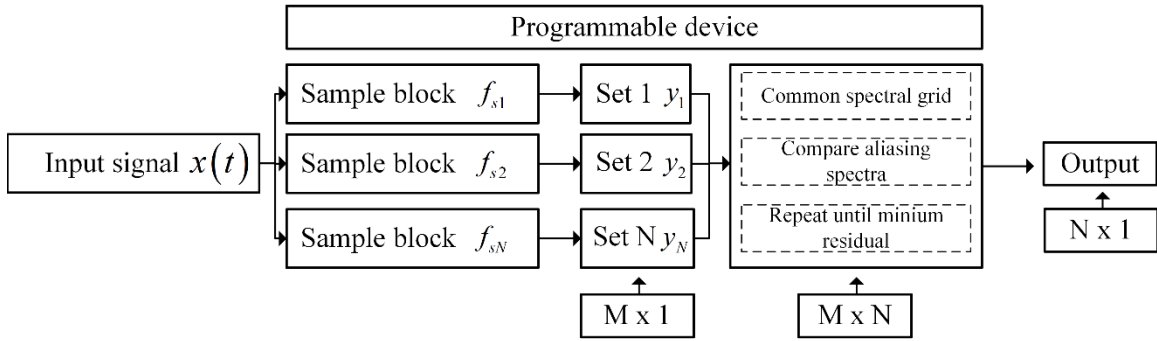


Figure 7. Asynchronous Multi-Rate Sampling Receiver.  
Adapted from [6].

The receiver operates by taking an input signal  $x(t)$ , constrained by a preselected bandwidth  $B$ , and samples it at the preset rates of its sampling blocks. A pre-selected number of samples  $M$  are taken from each sampling block to create the sampling sets. Each of the resulting sampling sets, designated by  $y_N$ , has a spectral grid spacing of  $f_{sN}/M$



where  $f_{sN}$  is the sampling frequency of the  $N$ th ADC channel. In [6], a method is provided for analyzing an undersampled signal by using the data in each sampling set. To accomplish this, a common spectral grid is created to account for the mismatched spectral grids of the sampling channels by dividing the input bandwidth into  $N$  commonly spaced grids. The value for  $B/N$  must be less than or equal to the minimum sampling frequency used. The spacing in the common spectral grid is given by [6]:

$$\text{Common grid} = \left[ 0, \frac{B}{2N}, \frac{2B}{2N}, \frac{NB}{2N} \right]. \quad (9)$$

After defining the common grid for use by all sampling sets, we can make an  $M \times N$  sensing matrix for each sampling frequency from the common spectral grid which acts as an inverse DFT matrix and is defined in [6] as

$$A_N = \begin{pmatrix} e^{-j2\pi t_N^1 (N-1)(B/N)} & \dots & e^{-j2\pi t_N^1 (N-1)(B/N)} \\ \vdots & \ddots & \vdots \\ e^{-j2\pi t_N^M (N-1)(B/N)} & \dots & e^{-j2\pi t_N^M (N-1)(B/N)} \end{pmatrix}. \quad (10)$$

The aliasing spectra are then calculated by taking the product of the conjugate transpose of the respective  $M \times N$  sensing matrix, designated by  $A_N$ , and its corresponding  $M \times 1$  undersampled vector, designated by  $y_N$ . The aliasing spectra are a representation of the horizontally concatenated frequency representations of the sampling channels using the common grid. When the aliasing spectra are obtained, an iterative process is run to obtain the active frequency bands and subtract the active component to create a residual waveform until the residual waveform is close to zero as described in [6].

### C. PHOTONIC COMPONENTS USED IN RADAR

In this thesis, only three photonic devices are used in concert with RF components to implement the compressive sensing-based radars: the Mach-Zehnder interferometer (MZI), photodiode detector, and a 1550 nm high power distributed feedback laser. The use of photonics in this research is limited, but photonic techniques have had an increasing use in radar systems. In [12] Ghelfi et al. created a fully photonics-based coherent radar system

able to transmit and receive up to 40 GHz with less than 15 fs of signal jitter and 10 fs of sampling jitter. The fully coherent photonic radar created in [12] outperforms state-of-the-art electronic transceivers by an order of magnitude. Their radar also includes a photonic-based ADC, and its increased precision allows it to achieve a greater estimation of range and speed estimation of targets. As requirements for radars and surveillance equipment increases, the utilization of photonics has the potential to become commonplace as they require less relative power and achieve higher rates of accuracy.

## **1. Laser Diodes and Photodiodes**

In this research, we use the optical beam created by laser diodes as the main method of information transfer in the receiver models. Specifically, a 1550-nm continuous wave, distributed feedback laser is used. A laser of this wavelength provides a bandwidth of 193 THz, which exceeds the capability of traditional electrical components and allows for the potential digitization of signals without the requirement of downconversion.

The signal analysis in this research is conducted in the RF domain. We use 1550 nm PIN type, high-speed fiber-optic detectors to convert the optical pulses into electrical current.

## **2. Mach-Zehnder Interferometer Modulator**

The main optical component in this research is the MZI which is used to manipulate the optical beam produced by the laser. The MZI has an input and output optical wave guide that is split and connected to two parallel waveguides as shown in Figure 8.

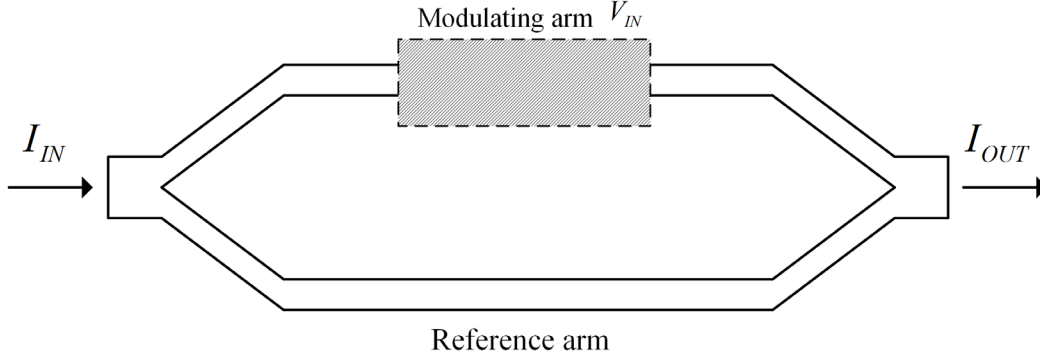


Figure 8. Mach-Zehnder Interferometer

When a voltage is applied to one side (modulating arm) of the parallel waveguides, a proportional phase shift is induced onto the light in the waveguide. The output is the result of the recombination of the light in the two parallel waveguides, and its intensity is proportional to the square of the combined field of the light in the parallel waveguides. If one side of the parallel waveguide is kept at a constant voltage, the resulting electrical field performs a modulating function. The output intensity is given by

$$I_{OUT} \propto \left| \frac{1}{\sqrt{2}} E e^{-i\phi_1} + \frac{1}{\sqrt{2}} E e^{-i\phi_2} \right|^2 = \frac{1}{2} (1 + \cos \Delta\phi) I_{IN} , \quad (11)$$

where  $E$  is the electric field,  $\phi$  is the phase,  $\Delta\phi = \phi_2 - \phi_1$ , and  $I$  is this the optical intensity. In (11), when the relative phase shift between the two parallel waveguides is  $\pi$  radians, the point on the modulator transfer function is minimum and the output is  $P_{MIN}$ . A typical MZI transfer-characteristic graph is shown in Figure 9. The modulators are used as both sampling devices to under sample the input signal and modulators to encode the RF information onto the optical pulses.

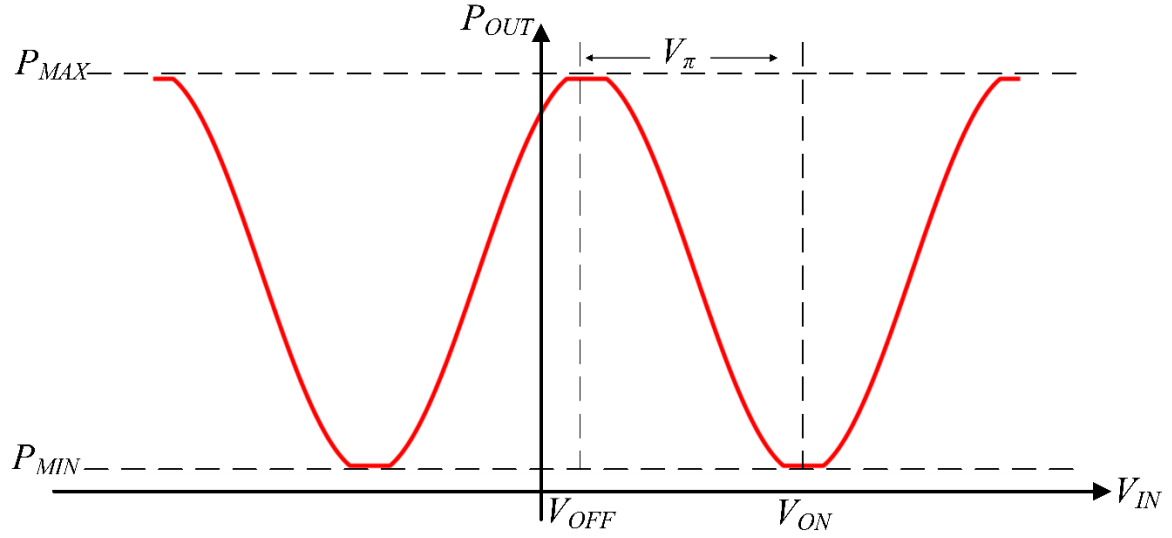


Figure 9. Mach-Zehnder Interferometer Transfer Characteristic Graph.  
Adapted from [13].

In this chapter, the different components and methods that are used in the modeling of the photonic A-to-I receivers were discussed. Optical modulators are used as both sampling devices and modulating devices to undersample signals in an attempt to recover information below the Nyquist rate.

### III. MATLAB SIGNAL PROCESSING SIMULATIONS

In this chapter, simulations carried out in MATLAB and in support of this research of the proposed photonic A-to-I receiver are presented. While the MATLAB simulations do not account for optical component performance, optical noise, power loss, or RF integration with optics, MATLAB does have the tools necessary to simulate the signal generation, undersampling, frequency analysis, sensing matrix construction, and signal recovery.

#### A. NYQUIST FOLDING RECEIVER SIMULATION

Several simulations were completed to demonstrate the function of the NYFR and note its limitations given selected parameters or signal environment. The block diagram of the NYFR MATLAB simulation is shown in Figure 10. The signal processing block of the MATLAB simulation consisted of both visual and algorithmic approaches to information recovery.

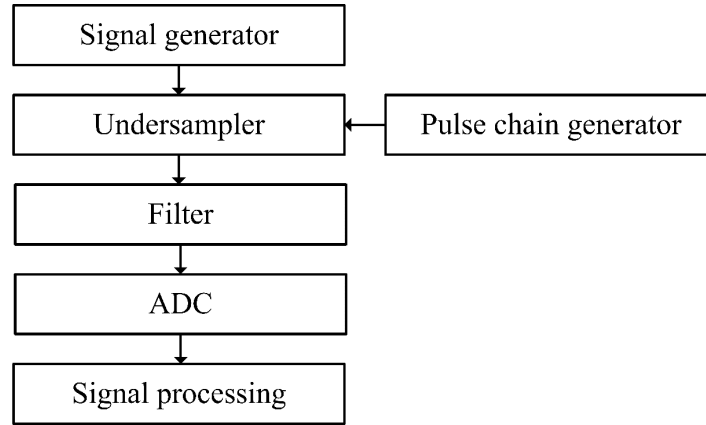


Figure 10. NYFR MATLAB Simulation Block Diagram

##### 1. Zero-Bandwidth, Zero-Noise Single-Tone Information Recovery

The first simulation was conducted using the parameters in Table 1 to verify single-tone frequency recovery of different input signal characteristics. The pulse train modulation is shown in Figures 11. Each Nyquist zone is the size of one-half of the center

frequency, 500 MHz. The sampling pulse harmonics begin to spill over into separate Nyquist zones at  $16 \cdot f_{s1}$ ; at this harmonic the sweep bandwidth will appear to be 0.8 GHz. In theory, this provides the frequency information in optimal conditions of a signal at less than 8% of the Nyquist rate.

Table 1. NYFR MATLAB Simulation Single Tone Recovery

Center Frequency $f_{s1}$	Sweep Bandwidth $f_{BW}$	Sweep Frequency $f_{ST}$	Interpolation Filter $f_{INT}$	ADC Frequency $f_{ADC}$
1 GHz	50 MHz	0.4 MHz	500 MHz	2 GHz

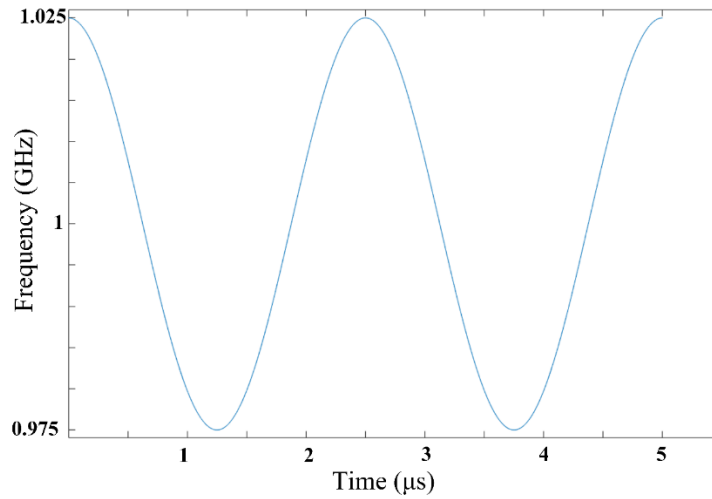


Figure 11. Sample Clock Modulation

A single tone of 1.15 GHz was used in the simulation to demonstrate the recovery of an undersampled signal. Using equations (4), (5), and (6), we determined that the undersampled signal had a scale factor of  $-1$  and a center frequency of 150 MHz. The spectrogram of the undersampled signal is shown in Figure 12.

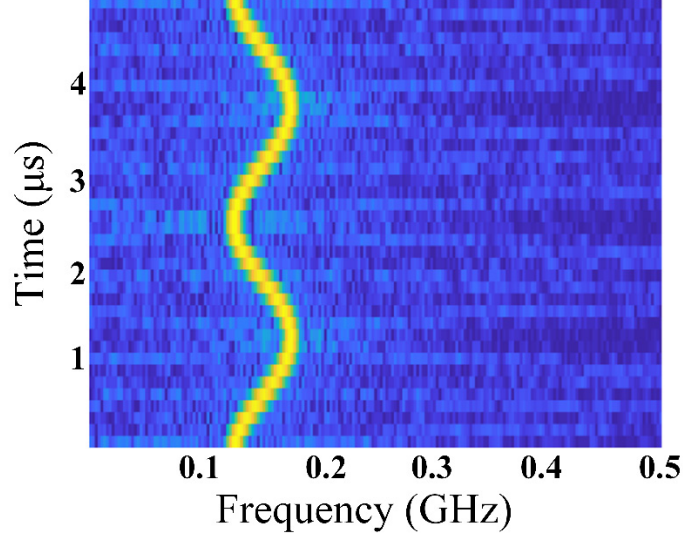


Figure 12. Frequency Spectrogram of Undersampled Signal  $f_I = 1.15$  GHz

If a priori information of the signal is not known, the recovered frequency can also be estimated in the time-frequency domain using the sampler pulse-modulation slope, the undersampled signal slope, the center frequency of the undersampled waveform, and the average sampling frequency of the pulse train [14]. Using equations (12) and (13) with a pulse slope of  $4 \cdot 10^{13}$  and signal slope of  $2.54 \cdot 10^{13}$ , we get the estimated input frequency of 1.15 GHz, which is equal to the input frequency. The modulation scale factor is given by

$$M = \text{round} \left[ \frac{\text{Signal Slope}}{\text{Pulse Slope}} \right]. \quad (12)$$

The input frequency can be calculated using the scale factor and the center frequency from [14]

$$f_{I,est} = f_{s1} \cdot |M| + \text{sgn}[M] \cdot f_{Center}. \quad (13)$$

Using visual recovery via the time-frequency domain is convenient and less computationally difficult for very sparse signal environments but quickly becomes more difficult as the environment becomes less sparse and noisier. Because the sensing matrix

created by Maleh in [4] enjoys the RIP, the frequency domain is able to be recovered using convex recovery methods. The MATLAB software package SPGL1, created by van den Berg and Friedlander, uses an algorithm to solve the basic pursuit (BP) problem

$$\underset{x}{\text{minimize}} \|x\|_1 \quad \text{subject to } Ax = b \quad (14)$$

and basic pursuit denoise (BPDN) problem

$$\underset{x}{\text{minimize}} \|x\|_1 \quad \text{subject to } \|Ax - b\|_2 \leq \sigma ; \quad (15)$$

where  $A$  is the sensing matrix,  $b$  is the undersampled signal,  $x$  is the Fourier domain of the unfolded signal, and  $\sigma$  is a positive value used to estimate the noise level [15]. Using the SPGL1 BP solver on 450 samples from the MATLAB NYFR simulation monitoring ten Nyquist zones of the undersampled 1.15 GHz signal produces the result shown in Figure 13. The 1.15 GHz was identified using the SPGL1 algorithm.

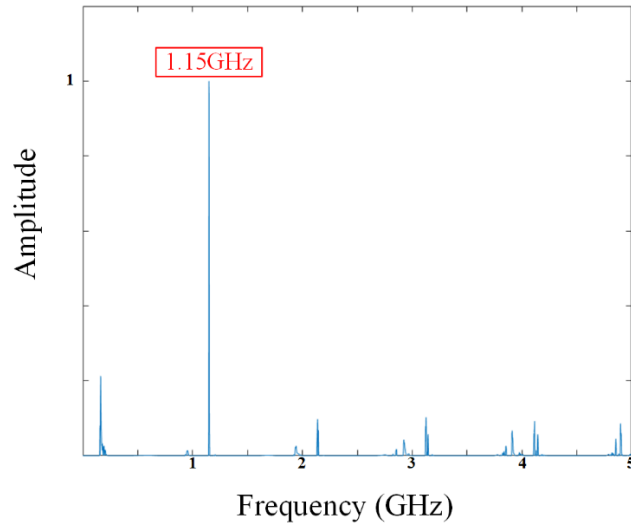


Figure 13. SPGL1 Algorithm Spectrum Recovery of 1.15-GHz Undersampled Signal



## 2. Zero-Bandwidth Noisy-Channel Single Tone Information Recovery

The next simulation was conducted to test the recovery of the same 1.15 GHz signal in a channel with additive white Gaussian noise (AWGN) included. The results for the recovery of a signal in a channel with a  $-12$  dB AWGN are shown in Figures 14 and 15. Visual information recovery via time-frequency analysis becomes less viable as the level of noise of the channel increases. It is important to note that this simulation run is also in the sparsest environment in which the receiver will operate. As the sparsity of the channel is reduced, visual recovery becomes untenable. The SPGL1 algorithm is also affected by the channel noise, but recovery of the signal's frequency information is still achievable. Additional signal processing steps can also be utilized to increase the probability of automated signal information recovery.

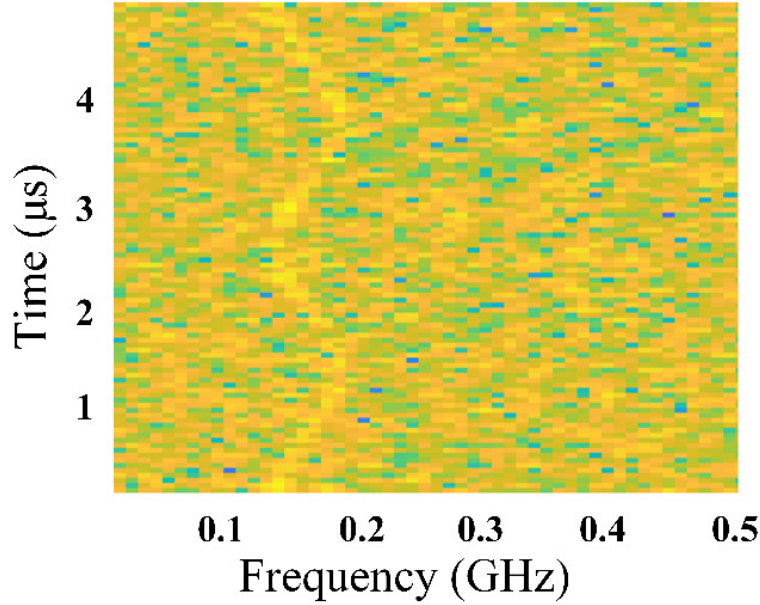


Figure 14. Frequency Spectrum of Noisy Undersampled  
Signal  $f_l = 1.15$  GHz

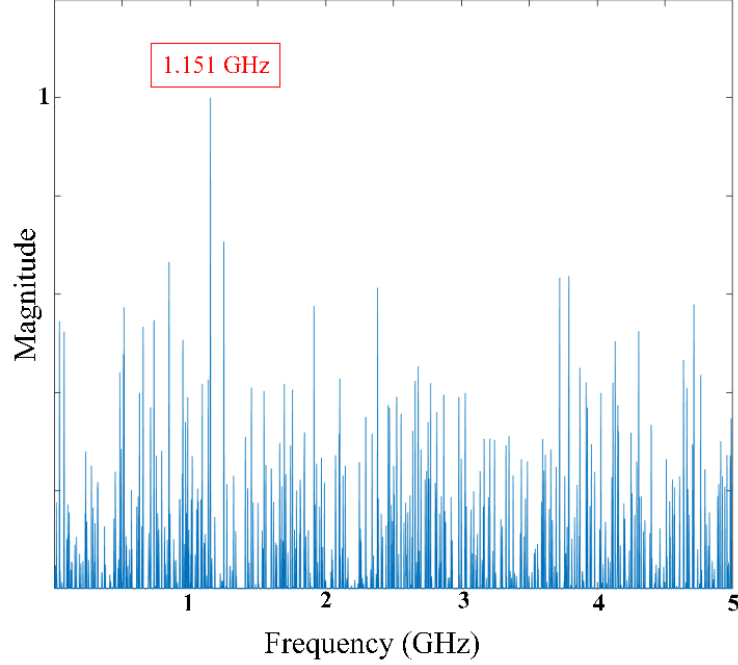


Figure 15. SPGL1 Algorithm Spectrum Recovery of 1.15-GHz Noisy Undersampled Signal.

Successful recovery of frequency information from the NYFR improves with the number of samples collected at the receiver. The result from Figures 13 and 15 are from samples of just 0.225  $\mu$ s. A dedicated processing unit can more efficiently complete information recovery and use longer sample periods. Through MATLAB simulation we observed that as the number of samples used for information recovery increased, the probability of successful Nyquist-rate information recovery also increased. Alternatively, in an automated detection scheme, as the signal environment became sparser, the chance of spurious frequency recoveries increased.

### 3. Zero-Bandwidth, Zero-Noise Multiple-Tone Information Recovery

A signal with multiple unit amplitude frequency tones was created and undersampled using the same parameters shown in Table 1. The frequency tones used and their corresponding Nyquist and Nyquist sampling rates are shown in Table 2. The sampling frequency used in the simulation for information recovery was 2 GS/s.

Table 2. NYFR MATLAB Simulation for Multiple Tones

Input Frequency	Nyquist Sampling Rate	Nyquist Zone	Percent Undersampled
1.15 GHz	2.3 GHz	2	13%
4.2 GHz	8.4 GHz	8	76%
9.3 GHz	18.6 GHz	19	89%
18.3 GHz	26.6 GHz	35	92%

The spectrogram of the undersampled multi-toned signal is shown in Figure 16. As can be seen, the manual recovery of frequency information becomes increasingly difficult as the sparsity decreases, and the corresponding Nyquist zone of the undersampled signal increases. On the other hand, the SPGL1 recovery algorithm was able to recover the all four frequency tones as shown in Figure 17.

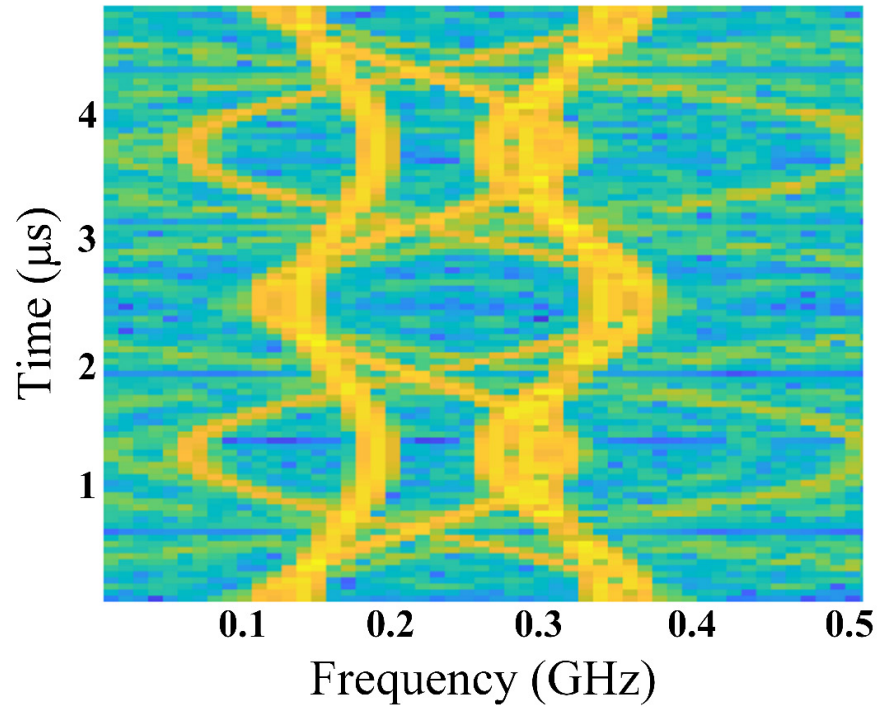


Figure 16. Frequency Spectrogram of NYFR Output for Signal Tones in Table 2

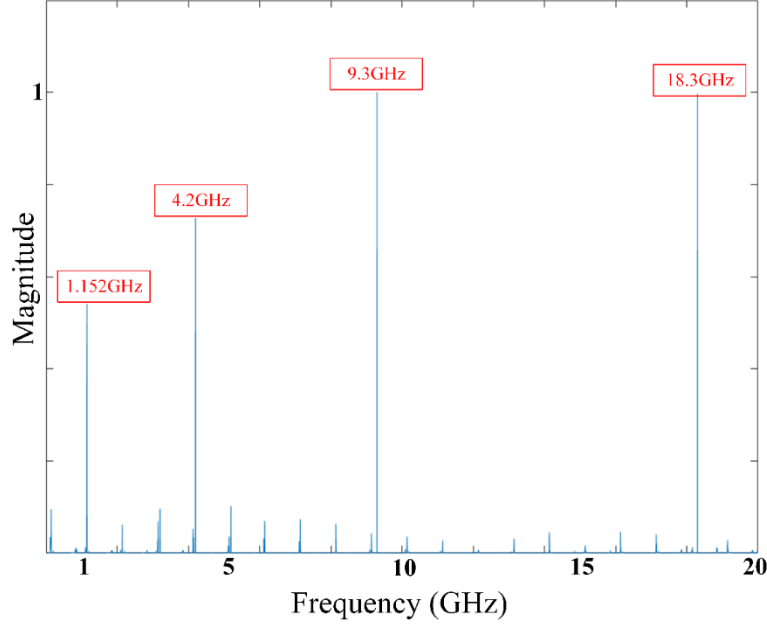


Figure 17. SPGL1 Algorithm Spectrum Recovery of NYFR Output for Signal Tones in Table 2

#### 4. Zero-Bandwidth, Noisy-Channel Multiple-Tone Information Recovery

The same four tones were sent through a channel with a  $-12$  dB AWGN. Although the Nyquist rate sampled signal frequency information is determined relatively easily as shown in Figure 18, extracting the frequency information from the NYFR output is more complex. Channel noise has a greater impact on the NYFR than a typical receiver. The SPGL1 recovery algorithm produces several frequency tones above the average noise level. The results from the NYFR output are shown in Figures 19 and 20. The SPGL1 recovery algorithm is more greatly impacted by the addition of noise in the ADC channel, introducing spurious frequency responses. This increases the level of difficulty in designing automatic information recovery methods. In Figure 20, the stars represent recovered signals automatic detection methods would have trouble recovering. The 10.3-GHz signal is a spurious frequency that would be identified by automatic methods.

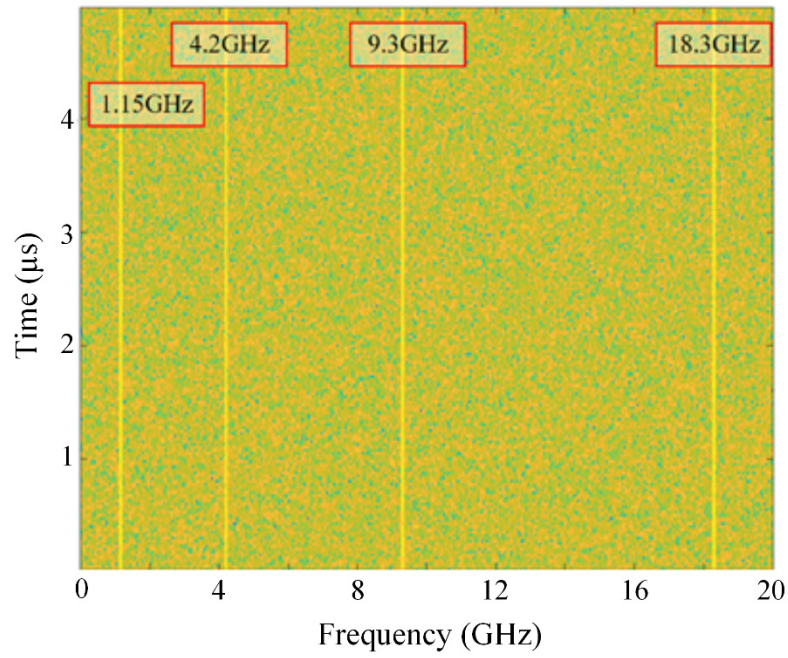


Figure 18. Nyquist Rate Sampled Spectrogram for Table 2  
Signals with Noise

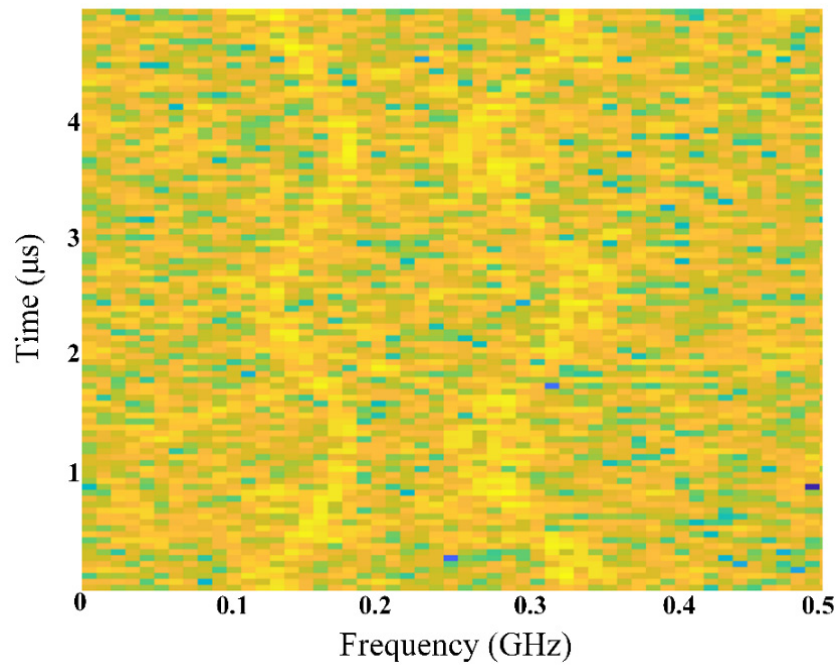


Figure 19. Undersampled Spectrogram for Table 2  
Signals with Noise

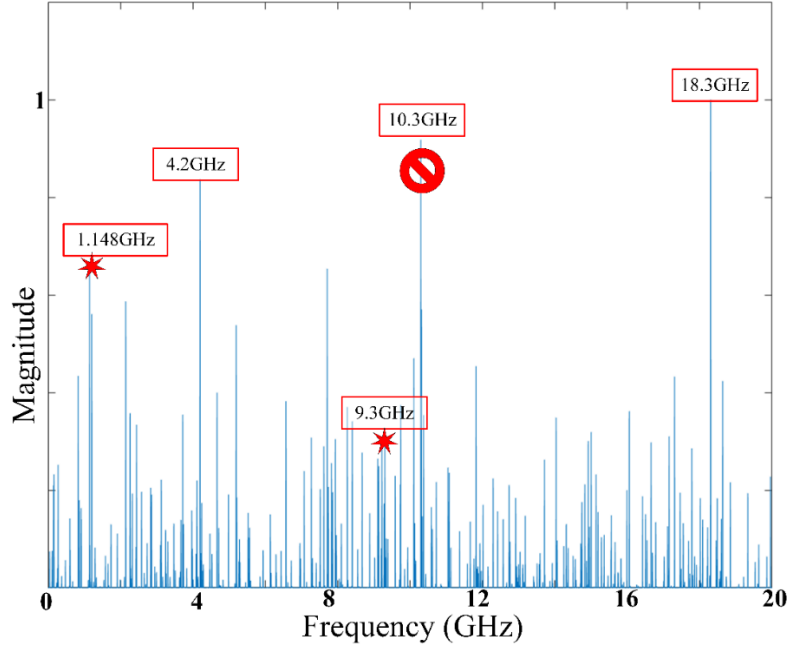


Figure 20. SPGL1 Spectrum Recovery for Table 2 Signals with Noise

## 5. Non-Zero Bandwidth Information Recovery

The NYFR encounters difficulty when faced with signals of significant bandwidth. Three simulations were conducted to show the difficulty in using the NYFR to process signals with significant bandwidth. The parameters of the simulations are shown in Tables 1 and 3. All of the simulations are sent through channels with zero noise.

Table 3. NYFR Simulation with Bandwidth Signals Parameters

Simulation #	Frequency Tone(s)	Bandwidth of Tone(s)
1	4.1 GHz	10 MHz
2	2.2 GHz	60 MHz
3	2.2 GHz 3.3 GHz	10 MHz 10 MHz

In the first simulation, a 4.1 GHz tone with a bandwidth of 10 MHz is sent through the NYFR. While the peak magnitude of the signal is recovered by the SPGL1 algorithm,

a general assumption can also be made about the signal's bandwidth, which is that the NYFR has produced artifacts in different harmonics of the sampling frequency. The results of the first simulation are shown in Figure 21.

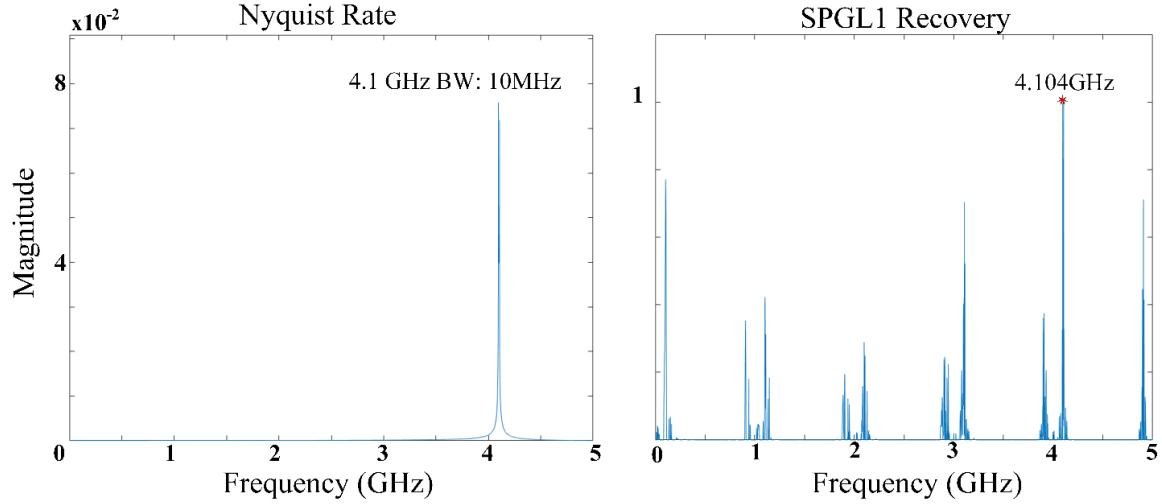


Figure 21. Nyquist Rate and NYFR Frequency Spectrum of Simulation #1 from Table 3.

In the second simulation, a 2.2-GHz tone with a bandwidth of 60 MHz is sent through the NYFR. This simulation was run to demonstrate the performance of the NYFR when the bandwidth of the collected signal is greater than the bandwidth of the sampler modulation. Again, the NYFR is able to detect the peaks of the Nyquist Rate signal but is unable to determine the bandwidth with any clarity. The results of the second simulation are shown in Figure 22.

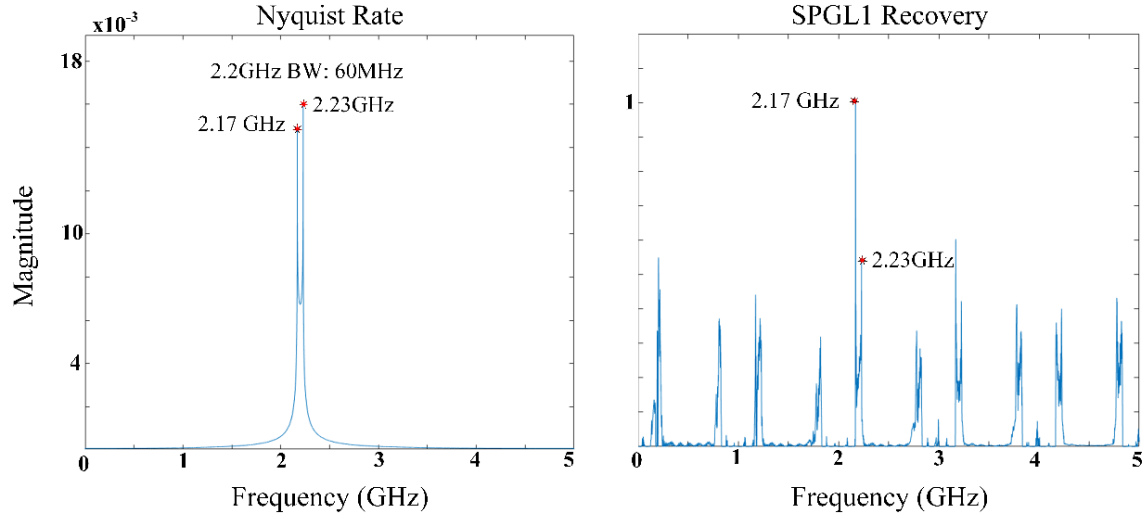


Figure 22. Nyquist Rate and NYFR Frequency Spectrum of Simulation #2 from Table 3.

In the third simulation, two 10-MHz wide tones are sent through the NYFR: 2.2 GHz and 3.3 GHz. This simulation was run to demonstrate the performance of the NYFR when in the reception of signals with bandwidth in a less sparse environment. The peaks of the Nyquist rate signals are recovered, but the potential for obtaining a spurious frequency has increased. The results of the third simulation are shown in Figure 23.

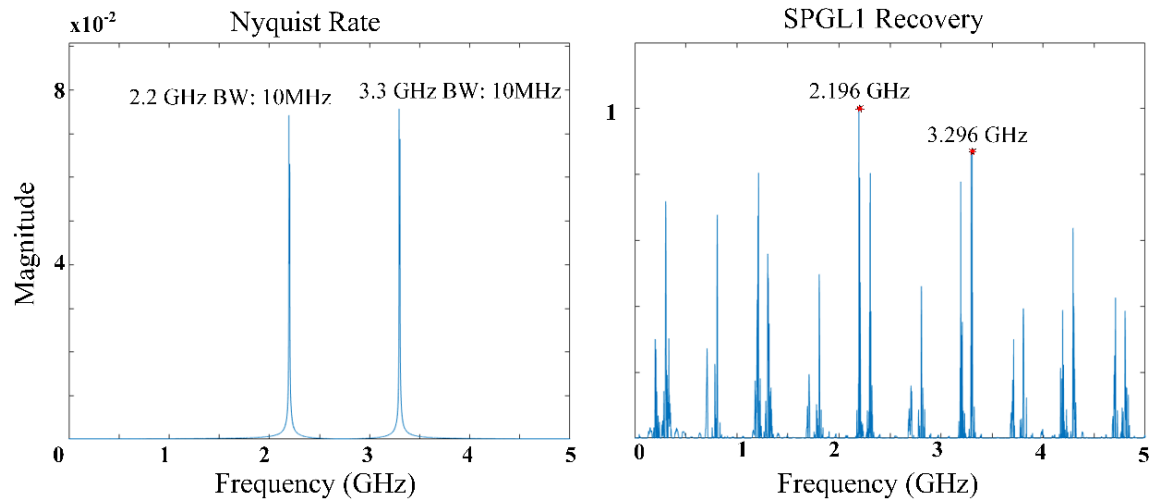


Figure 23. Nyquist Rate and NYFR Frequency Spectrum of Simulation #3 from Table 3.



The simulations covered in this section demonstrate the functionality and some of the limitations of the NYFR which is able to achieve frequency information recovery at a rate significantly lower than the Nyquist rate. The NYFR model encounters limitations when the signal environment is less sparse and when signals with significant bandwidth are present in the environment.

## B. ASYNCHRONOUS MULTI-RATE SAMPLING RECEIVER

Simulations were completed of the asynchronous multi-rate sampling receiver described by Tzou in [6] to demonstrate its functionality and note its limitations. The block diagram of the MATLAB simulation is shown in Figure 24. Tzou describes two steps to recover frequency information from the undersampled signals: detect the active band and use a relatively smaller number of samples, followed by using the results of the active band detections to reconstruct the spectrum using a significantly greater number of samples. In [6], Tzou used 16,384 samples to reconstruct the undersampled signal. In this thesis, the aim is to simply demonstrate basic functionality of this undersampling technique, so a hybrid method of both detecting the active bands and recreating the spectrum in one iterative loop is used.

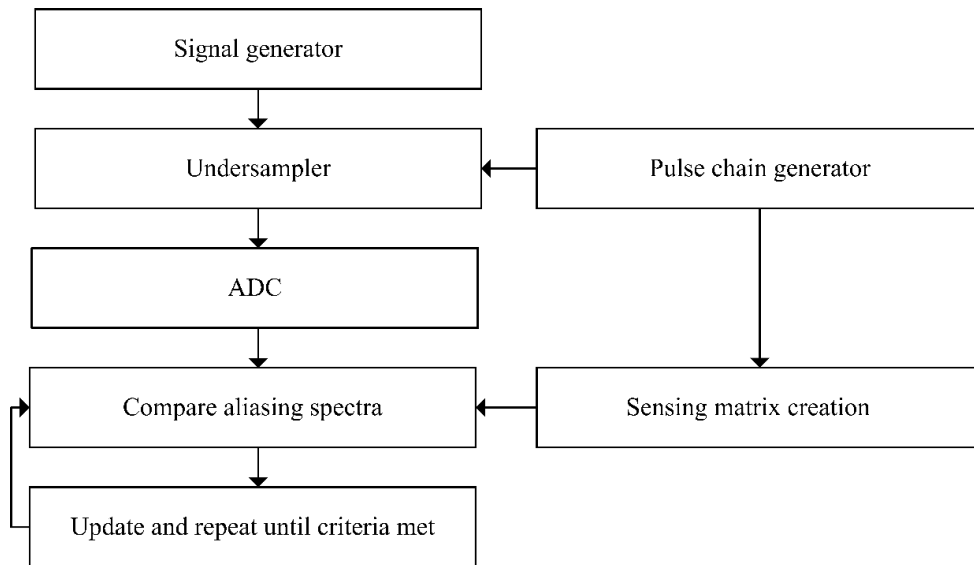


Figure 24. Asynchronous Multi-Rate Sampling Receiver  
MATLAB Block Diagram

The *Sensing matrix creation* block uses the pulse times from the pulse chain generator for each sampling frequency to create the sensing matrices according to (12). The *Compare aliasing spectra* block takes the product of each undersampled channel with its respective sensing matrix and compares each aliasing spectra to find the section of the frequency spectrum with the highest energy level. In the *Update and repeat* block, this section of the frequency spectrum is removed from each respective channel, and the process is repeated until user input criteria are met. In this simulation the criteria for stopping is a number a preselected number of loops.

For the first simulation, four signals, a 0.3 GHz tone, a 1.6 GHz tone, a 2.31 GHz tone, and a 3.76 GHz tone, are sent through the multi rate sampling receiver. Four sampling channels are used giving an average sampling rate of 1 GHz. This simulation was conducted to demonstrate the capability of recovering sparse frequency tones. The receiver parameters are listed in Table 4. The time-domain representation of the original signal and the corresponding sampling points is shown in Figure 25.

Table 4. Asynchronous Multi-Rate Receiver Simulation Parameters

Bandwidth	No. Samples	Sampling Channel Frequencies (GHz)
5 GHz	1000	0.8, 0.9, 1.1, 1.2

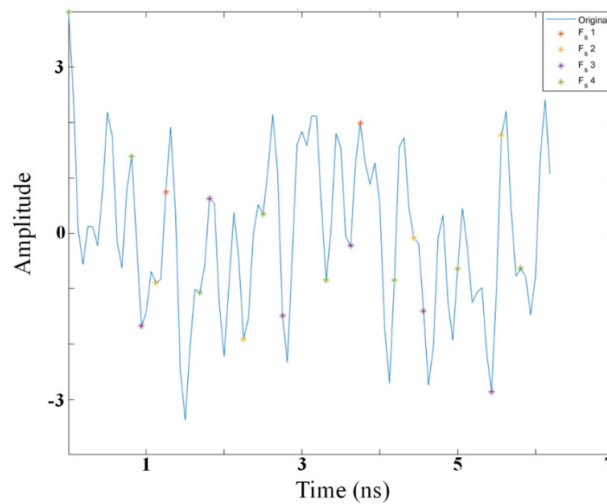


Figure 25. Original Signal with Corresponding Undersampling Points

The undersampled frequency spectrum of each channel is shown in Figure 26. As expected, the only frequency tone able to be recovered in the undersampled channels is at 300 MHz. All four sampling channels meet the Nyquist criteria for this signal. The aliasing spectra for each sampling channel, which is a horizontal concatenation of the common grid frequency response, is shown in Figure 27.

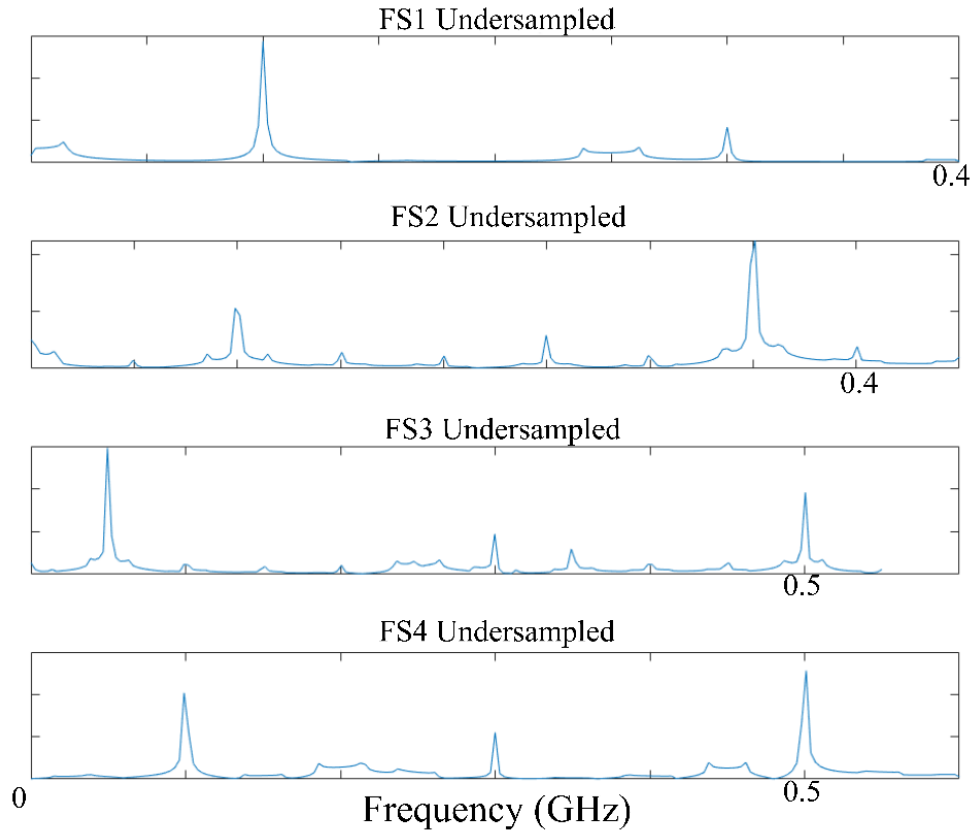


Figure 26. Undersampled Channel Frequency Spectrum

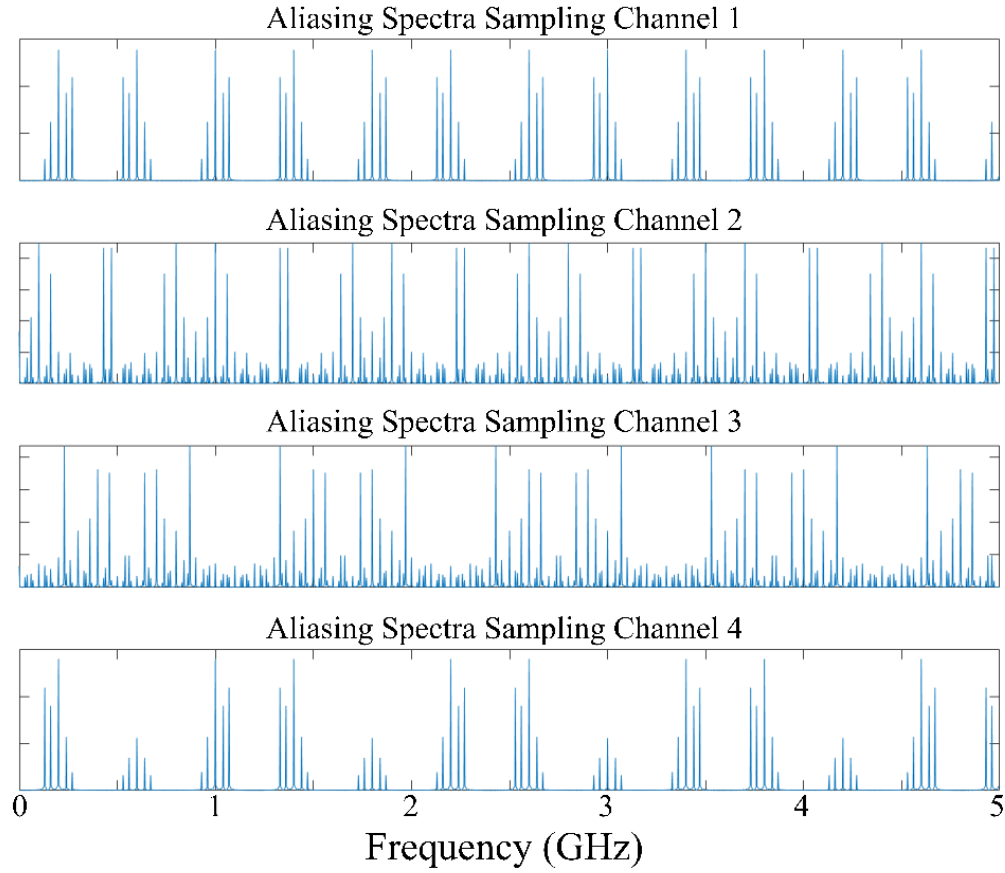


Figure 27. Sampling Channel Aliasing Spectra

The output of the aliasing spectra of Sampling Channel 1 after the input criteria for iteration completion is met is shown in Figure 28. Further automation of the receiver requires the completion of spectrum correlation and variation between the aliasing spectra to decide which spectra best reconstructs the Nyquist rate signal characteristics. For this research, visual identification of the most accurate aliasing spectra is sufficient. All of the input frequencies were recovered. Some spurious frequencies are recovered in the aliasing spectra.

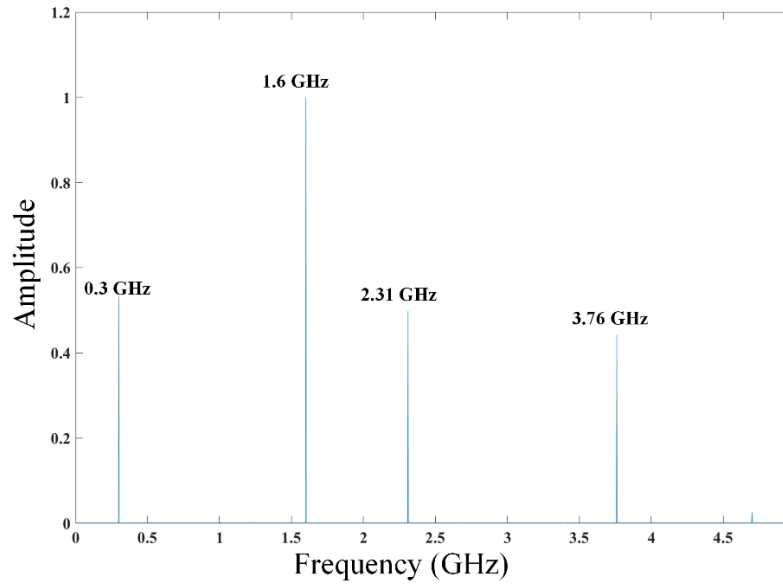


Figure 28. Sampling Channel 1 Aliasing Spectra

The same four-tone signal was sent through a channel with  $-6$  dB AWGN. While there are additional spurious frequencies at the output of the receiver, all of the input frequencies were successfully recovered. Given more samples, the clarity of the receiver output would increase. The result is shown in Figure 29.

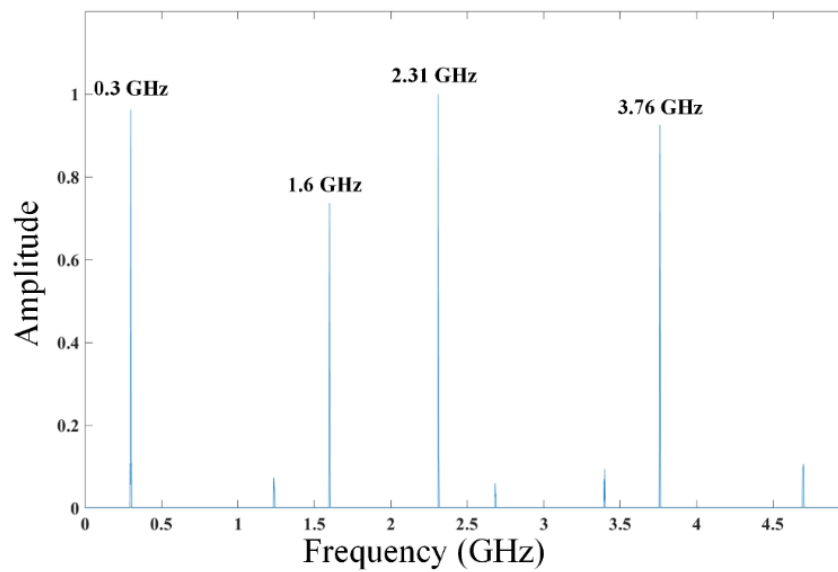


Figure 29. Sampling Channel 4 Aliasing Spectra

The next simulations conducted determined the ability of the receiver to recover signals with non-zero bandwidth. In the first simulation, a 2.34-GHz signal with a bandwidth of 60 MHz and no AWGN was used. The receiver had the same parameters as in Table 4, but the number of samples taken was increased to 2000. The results of the simulation are shown in Figure 30. The receiver does not perfectly reconstruct the Nyquist rate sample, as seen in Figure 30b, but the accuracy of the reconstruction is tied to the quantity of samples.

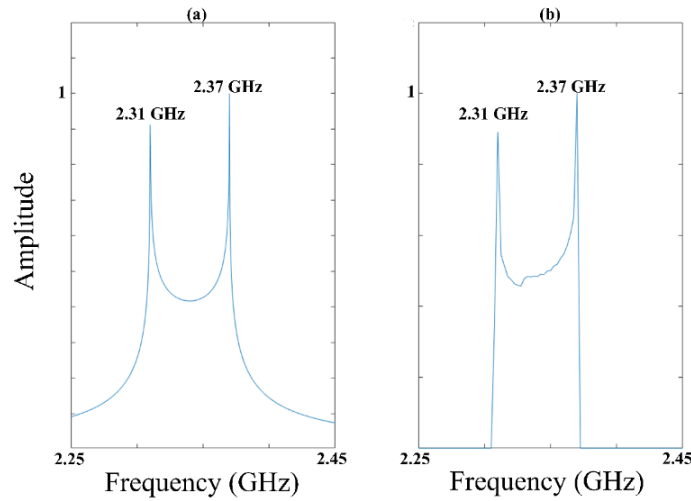


Figure 30. (a) Nyquist Rate Spectrum Sample (b) Sampling Channel 3 Aliasing Spectra

Next, the receiver's ability to reconstruct multiple signals with bandwidth was tested. Three 40-MHz wide signals were sent through the receiver at 1.33 GHz, 2.6 GHz, and 3.76 GHz. Additional receiver input adds complexity to the reconstruction process and increases the rate of spurious frequencies detected. The reconstructed frequency information of the Nyquist rate input signals were able to be recovered at a lower level of accuracy. The results are shown in Figures 31 through 33, which indicate that the proposed receiver is capable of recovering undersampled information for signals with non-zero bandwidth.

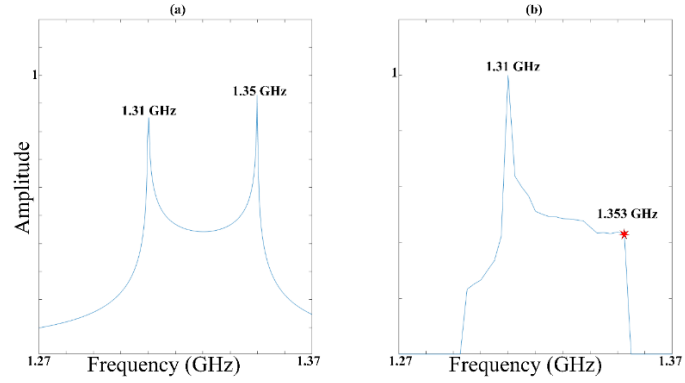


Figure 31. 1.33-GHz BW: 40 MHz (a) Nyquist Rate Spectrum Sample (b) Aliasing Spectra

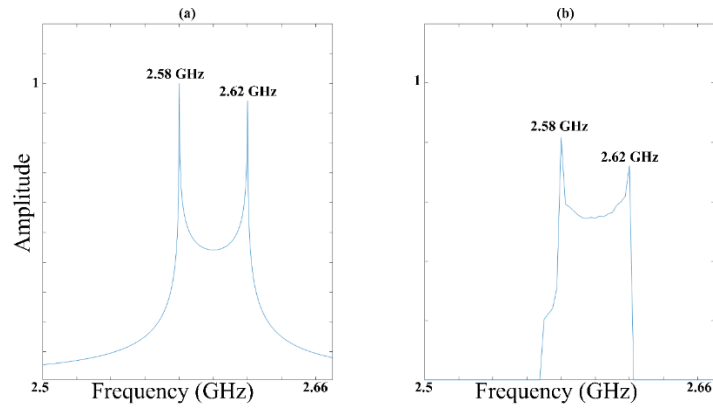


Figure 32. 2.6-GHz BW: 40 MHz (a) Nyquist Rate Spectrum Sample (b) Aliasing Spectra

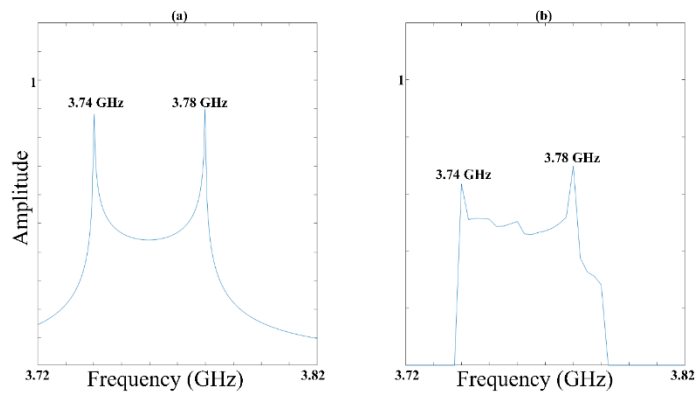


Figure 33. 3.76-GHz BW: 40 MHz (a) Nyquist Rate Spectrum Sample (b) Aliasing Spectra

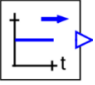
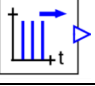
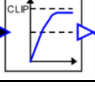
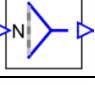

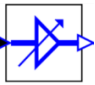

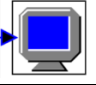
THIS PAGE INTENTIONALLY LEFT BLANK.

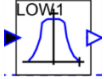
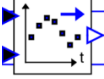
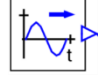
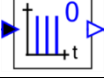
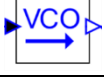
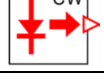




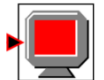
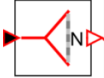
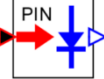
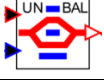


## IV. OptSim HARDWARE SIMULATIONS

In support of this thesis research, an experimental hardware prototype of a portion of the NYFR receiver using photonic components was developed; this work is presented in a later chapter. In this chapter, the simulation of the photonic experiments using a simulation tool known as OptSim is described. OptSim is an optical communications system simulation package created by Synopsys Inc. which can be used to model, design, and simulate photonic systems. OptSim has predefined hardware building blocks that can be integrated into complex models to predict the performance of the hardware prototype. [13]. In this thesis, ideal hardware models were created to verify the performance of the analog-to-information methods using optical components. The OptSim models used in this simulation are described in Table 5.

Table 5. OptSim Hardware Model Description. Source: [13].

Model Image	Model Name
	Bias Signal Generator
	Clock Signal Generator
	Electrical Clipper
	Electrical Combiner
	Electrical Connection
	Electrical Gain
	Electrical Probe Connection
	Electrical Scope

Model Image	Model Name
	Low-pass Filter
	Sampler
	Sinusoidal Wave Signal Generator
	Timing Pulse Generation on Zero Crossing
	Voltage Controlled Oscillator
	Continuous Wave Laser
	Fixed Gain Optical Amplifier
	Linear Amplitude MZI
	Optical Connection
	Optical Probe Connection
	Optical Probe
	Optical Splitter
	Photodiode
	Unbalanced Single Arm MZI

### A. SINGLE-SOURCE PHOTONIC NYFR

In [5], Shmel designed several prototype photonic NYFRs. His most promising design consisted of an external pulse train generator, a MZI to create the optical pulse train, a second MZI to modulate the RF onto the optical pulses and perform the undersampling, and a photodiode to turn the optical pulses into electrical current for digitization. Shmel relied on image analysis of the time-frequency domain to recover unfolded signal information from the NYFR. In this research, small improvements in the pulse generation and RF modulation schemes of the modulators were made to aid in the recovery of signal information by compressed sensing techniques. The OptSim model of the single-source photonic NYFR is shown in Figure 34.

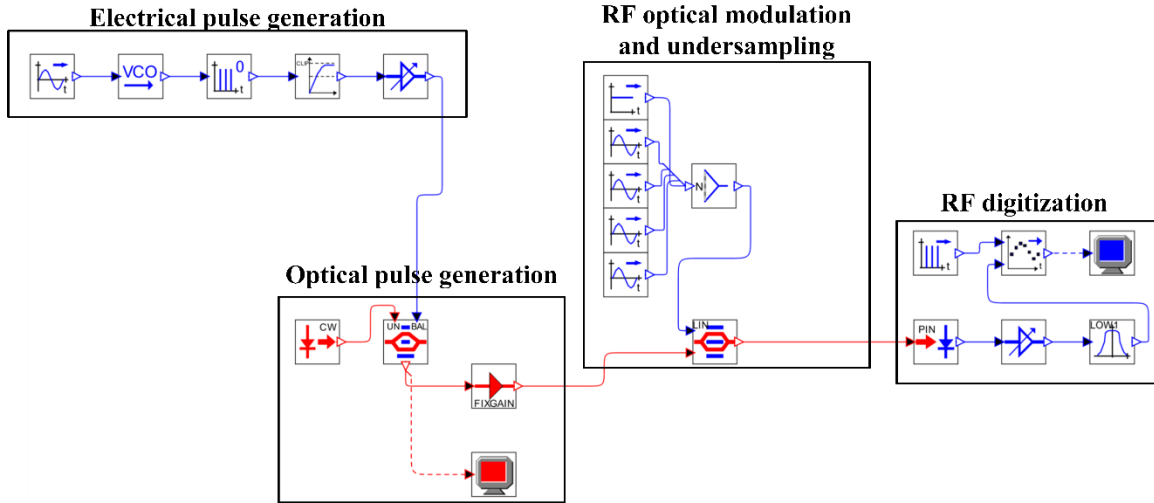


Figure 34. OptSim Model of Single-Source Photonic NYFR

In the *Electrical pulse generation* block, a sinusoidal wave representing  $\theta(t)$  from (4) is fed into a voltage-controlled oscillator to create the frequency-modulated wave used for the pulse generation. The pulse is generated by a zero-crossing generator and then clipped to an amplitude of 1V by an electrical clipper to ensure uniform pulses. The clipped pulse is amplified to 5 V, which corresponds to the maximum intensity response of the MZI in the optical pulse generation block. The accuracy of the optical signal representation is directly related to the uniformity of the pulses generated in the optical pulse generator.

By taking measures to ensure a uniform electrical pulse prior to the optical pulse generation block, we increased the uniformity of the optical pulse generation.

The *Optical pulse generation* block consists of a continuous-wave laser source that is always on. The laser in the simulation is transmitting 5 mW of optical power at a wavelength of 1550 nm. The MZI in this block has the same transfer characteristic graph as shown in Figure 9 and produces no optical output when the input amplitude is 0 V. When it receives the pulse of amplitude 5 V, it produces the maximum output optical power for the duration of the pulse. The sampling block models provided in OptSim enabled the creation of an extremely narrow pulse with little variation in voltage, which is shown in Figure 35.

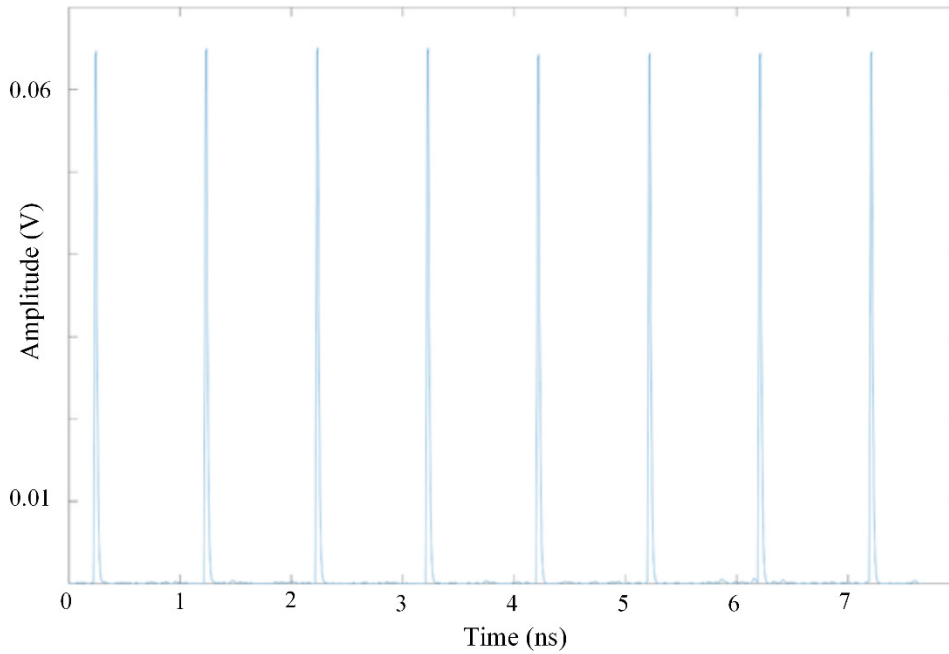


Figure 35. OptSim Pulses at Output of MZI

The *RF optical modulation and undersampling* block consists of a linear amplitude MZI and RF input. The linear amplitude modulator is chosen to better represent the input RF signal in the optical domain. The antenna signal is modeled by a four-tone source. The total source input is limited to 1-V peak-to-peak and a bias signal of amplitude 1 V is

combined with the source. This combination creates an input to the modulator of 1 V peak-to-peak with a DC offset of 1 V. This produces the most accurate RF signal representation in the optical domain. The linear amplitude MZI's transfer characteristic graph with noted bias point is shown in Figure 36.

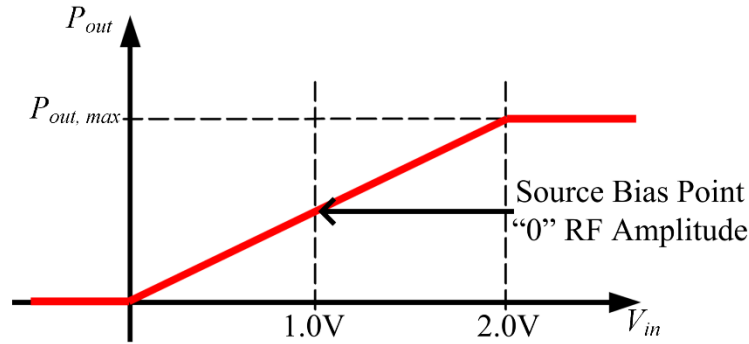


Figure 36. Linear Amplitude MZI Transfer Characteristic Graph.  
Adapted from [13].

The *RF digitization* block begins with the photodiode, which is used to turn the optical pulses into electrical current. The output of the photodiode is amplified and fed through a low-pass filter which serves as the interpolation filter. The output of the low-pass filter is then fed through a sampler, which is controlled by a clock generator. The output of the NYFR is retrieved from the electrical scope. An OptSim simulation was run to test the operation of this NYFR using the settings in Table 6.

Table 6. Single Source Photonic NYFR Simulation Parameters

Center Frequency $f_{s1}$	Sweep Bandwidth $f_{BW}$	Sweep Frequency $f_{ST}$	Interpolation Filter $f_{INT}$	ADC Frequency $f_{ADC}$
1 GHz	50 MHz	0.4 MHz	500 MHz	2 GHz

The source signal contained the following frequency tones: 1.6 GHz, 4.1 GHz, 6.33 GHz, and 9.8 GHz. The SPGL1 recovery of the NYFR output in a channel with no noise

is shown in Figure 37. Because of the biasing required in the modulators, a strong tone is recovered at 0 Hz, which can lead to difficulties in the recovery of signals in a noisy channel.

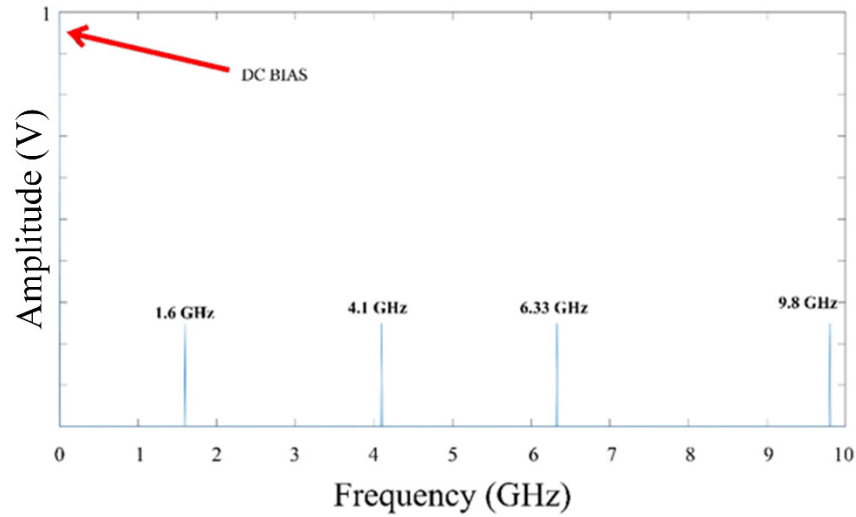


Figure 37. OptSim Simulation SPGL1 Recovery

The simulation was run again in a channel with uniform noise of equal level to the combined tones. The SPGL1 recovery result is shown in Figure 38. The DC bias is not impacted by the channel noise and increases the difficulty of recovery. The SPGL1 recovery with the DC bias filtered out is shown in Figure 39. In this signal environment, it is very difficult to automatically recover information using this approach.

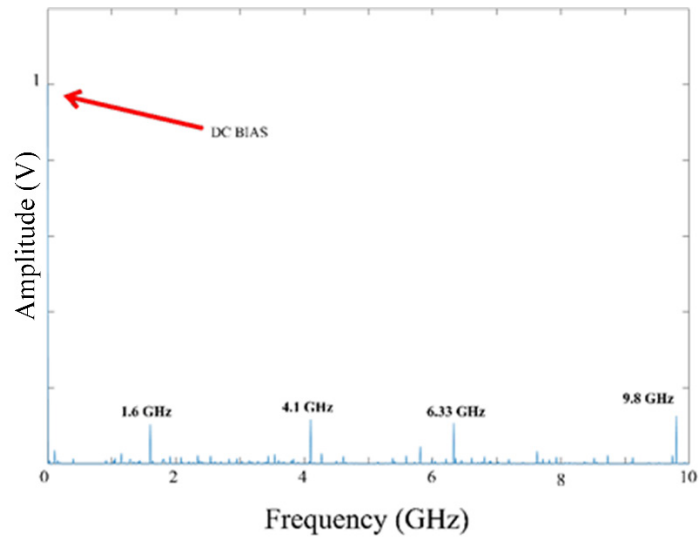


Figure 38. OptSim Simulation SPGL1 Recovery with Noise Added

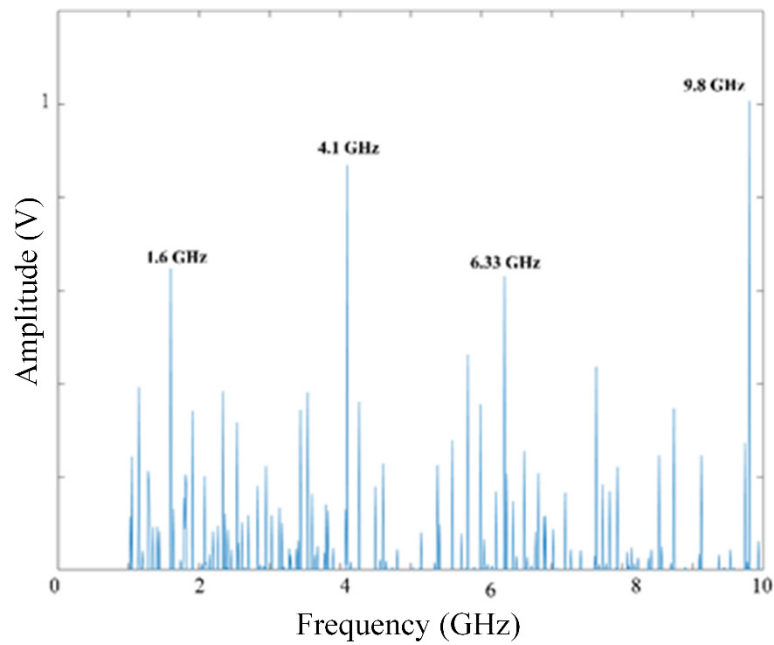


Figure 39. OptSim Simulation SPGL1 Recovery with Noise and Filtered Bias

The OptSim simulations showed that the photonic NYFR is capable of recovering undersampled frequency information but with some difficulty. There are several power

management and biasing techniques required that add to both the optical and RF noise in the environment.

## B. PHOTONIC ASYNCHRONOUS MULTI-RATE SAMPLING RECEIVER

The asynchronous multi-rate receiver proposed by Tzou in [6] was modeled in OptSim. The pulse generation method used in this receiver is similar to the method used in both photonic NYFR models discussed previously. Because there is no requirement for a phase modulated pulse train, the voltage-controlled oscillator is not used. The input to the zero-crossing generator is a sinusoid with frequency set to the sampling channel frequency. Two MZI modulators are required for each sampling channel, one to create the optical pulse and the other to modulate the RF into the optical domain. Additional optical amplifiers are required for each pulse generation block. The OptSim model is shown in Figure 40.

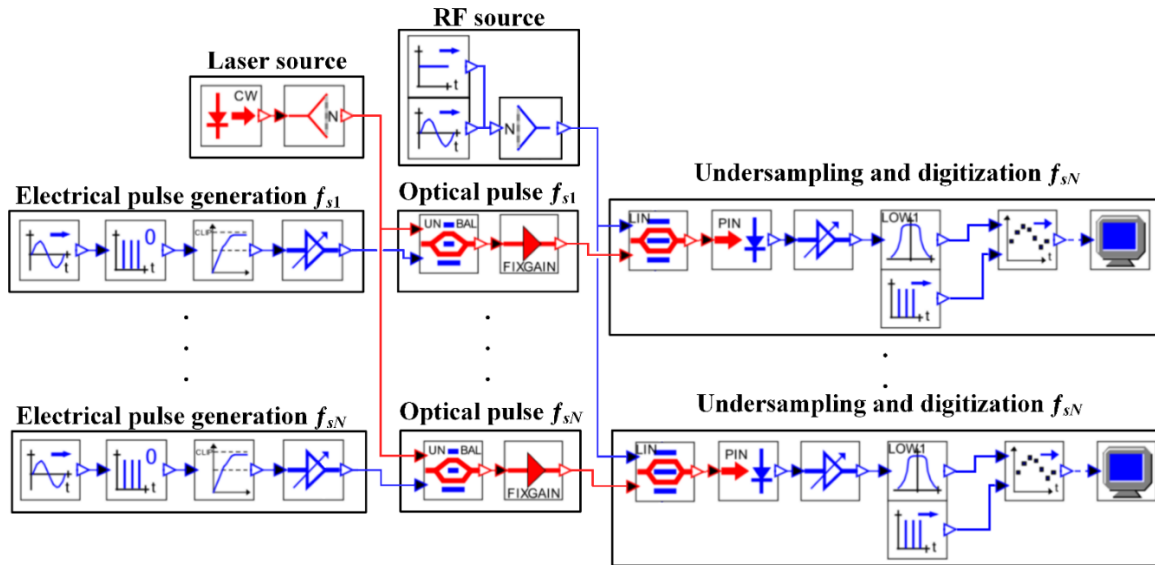


Figure 40. OptSim Model of Multiple Rate Receiver

A simulation was conducted with zero-bandwidth tones of 0.95 GHz, 1.45 GHz, and 1.8 GHz to verify the performance of the photonic asynchronous multi-rate sampling receiver. The parameters used for the simulation are shown in Table 7.



Table 7. OptSim Multi-Rate Receiver Simulation Parameters

Bandwidth	No. Samples	Sampling Channel Frequencies (GHz)
5 GHz	2000	0.8, 0.9, 1.1, 1.2

The multi-rate receiver relies on precise samples and their corresponding time values to calculate the aliasing spectra and reconstruct the Nyquist rate sample. In order to accomplish this with photonics, ADC synchronization with the pulse train and modulator is vital. The results from one sampling channel are shown in Figure 41. The ADC could not be synchronized with the optical pulses in the simulation, which resulted in poor results post ADC. For purposes of this research, the modulator output and processing methods in MATLAB was used to get a more accurate representation of the samples acquired.

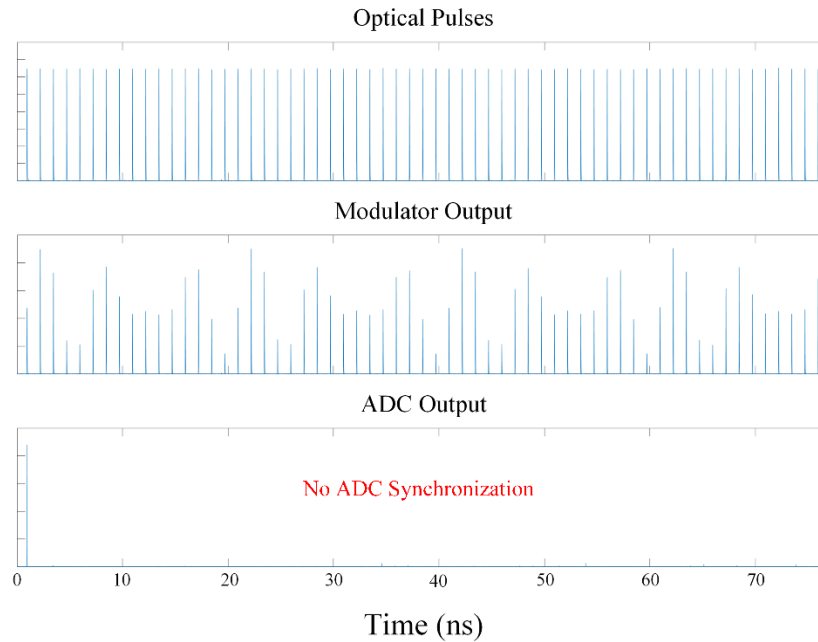


Figure 41. OptSim Multi-Rate Receiver Sampling Channel 1 Results

With the samples and times obtained from the modulator output, the aliasing spectra were able to be constructed. The aliasing spectra results were not as accurate as the results obtained from the MATLAB simulation. The output of the MZI modulator used for the

pulse train does not create an ideal sampling pulse as shown in Figure 42. Not all of the correct input frequencies were able to be recovered in the aliasing spectra. This may have been a result of the imprecise samples and sampling times obtained using the photonic components and the DC bias used on the modulators. With adequate pulse train and ADC synchronization and an increased number of samples, the results may improve. The aliasing spectra are shown in Figure 43. The spurious frequency results may be the result of sampling pulse and timing inconsistencies. Further experimentation using photonics to implement the asynchronous multi-rate sampling receiver is required to make a better determination of its functionality. A simulation model with correct ADC synchronization was not able to be implemented.

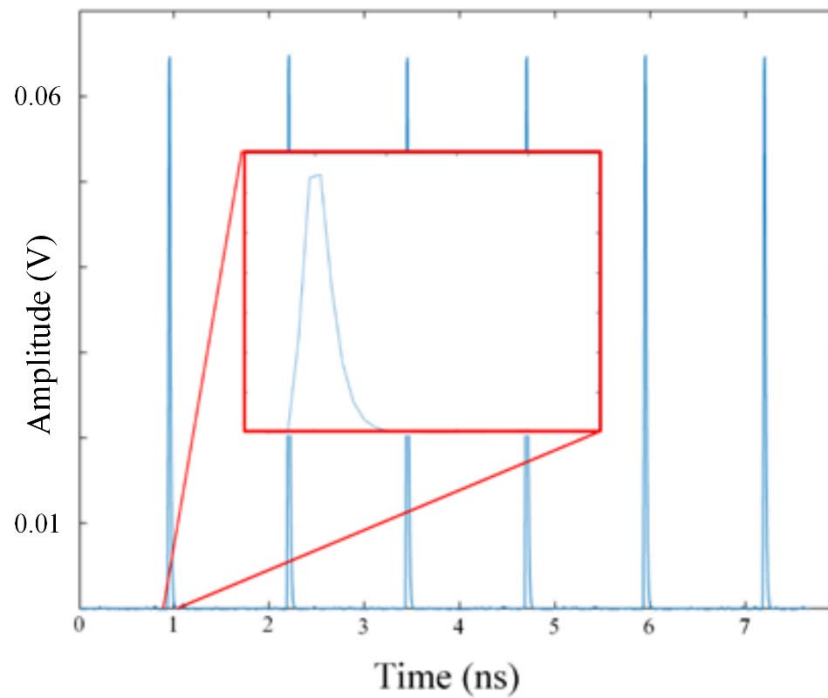


Figure 42. OptSim Multi-Rate Receiver Sampling Pulse Shape

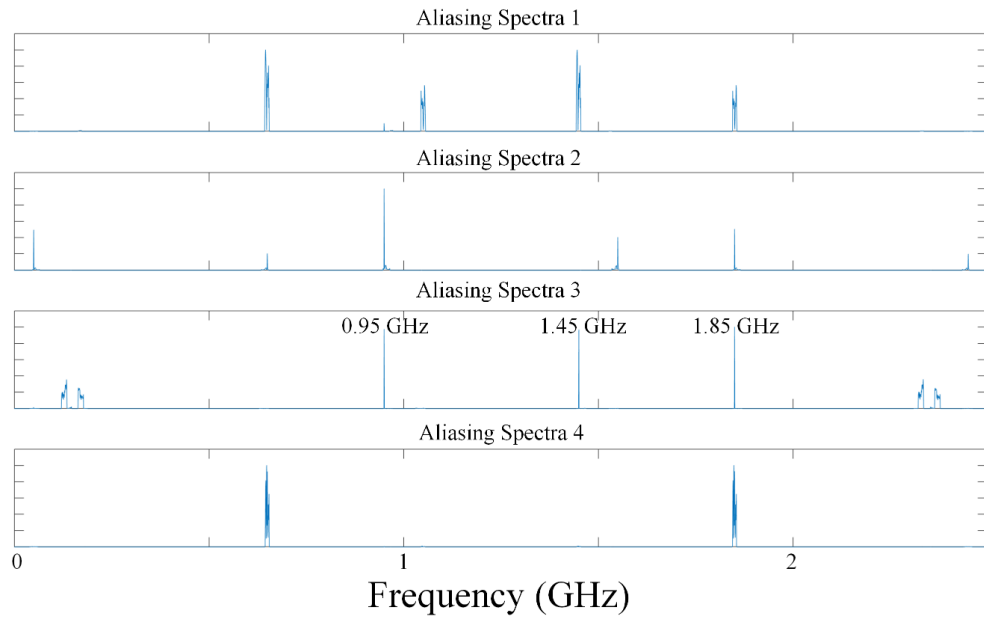


Figure 43. OptSim Multi-Rate Receiver Aliasing Spectra

THIS PAGE INTENTIONALLY LEFT BLANK.

## V. PHOTONIC A-TO-I RECEIVER HARDWARE TESTS

Multiple tests were conducted using commercial-off-the-shelf components to assess the performance of the photonic NYFR receiving models created in OptSim. The goal of these tests was to recover signal information using samples acquired below the Nyquist rate using the compressive sensing model created by Maleh in [4]. The tests were limited to the maximum useful frequency range of the 20-MHz function generator. Ultimately, recovering information using the compressed sensing model was unsuccessful, but valuable insight was gained into the performance of the photonic components involved. The equipment used while conducting these tests is listed in Table 8.

Table 8. Laboratory Test Equipment

Label #	Model Name
1	THORLABS ITC510 Laser Diode Combi Controller
2	740 Series Telecom Laser Diode Mounts Gooch & Housego High Power Distributed Feedback Laser
3	SN74121 Monostable Multivibrator
4	Power Supply
5	Agilent 33220A 20 MHz Function/Arbitrary Waveform Generator
6	Tektronix DPO 4034 Digital Phosphor Oscilloscope
7	Newport D-30ir Detector
8	THORLABS 500 kHz Low Pass Filter
9	PE1606 SMA Bias Tee
10	JDSU Optical Linearized Modulator
11	JDSU X5 Single Drive Optical Modulator
12	HP 8347A RF Amplifier

## A. LINEARIZED MODULATOR NYFR TESTS

In [5], Shmel implemented a prototype NYFR using two MZI modulators and a Laser Safety Class 1 laser that provided 1.75 mW. The pulse train was created by feeding a square wave to a monostable multivibrator that produced a pulse at the edge of the square wave. In order to ensure accurate signal representation at the output of the photonic NYFR, we first sought to increase the power at the laser source and minimize the power loss in the receiver design. To implement this, a Laser Safety Class 3b laser capable of producing 100 mW and an optical linearized modulator were used.

The optical linearized modulator is a single unit with two cascaded MZI modulators with independent biases. There is an RF input for each modulator and an inverted and non-inverted output. The modulator and its block diagram are shown in Figure 44.

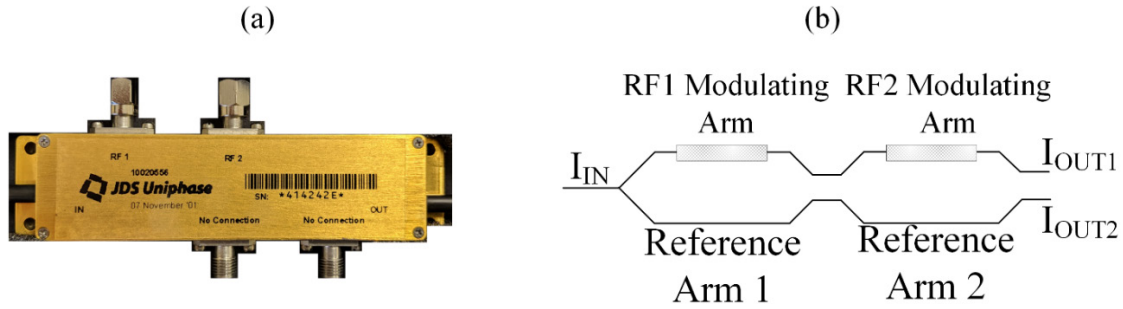


Figure 44. JDSU Optical Linearized Modulator

The laboratory setup for these tests is shown in Figure 45. A function generator to generate a square wave to use as the input to the multivibrator to create a RF pulse was used. Because the linear optical modulator has no voltage bias connections, the PE1606 bias tee was required to produce the bias necessary for the modulator. The output of the bias tee was connected to RF1. The second function generator was used as the modulating waveform and was connected to the RF2. One of the modulator outputs was connected to the photodiode whose output was connected to either the low-pass filter and then to the oscilloscope. For experiments in determining the specific output of the modulator, the low-

pass filter was removed, and the output of the photodiode was connected directly to the oscilloscope.

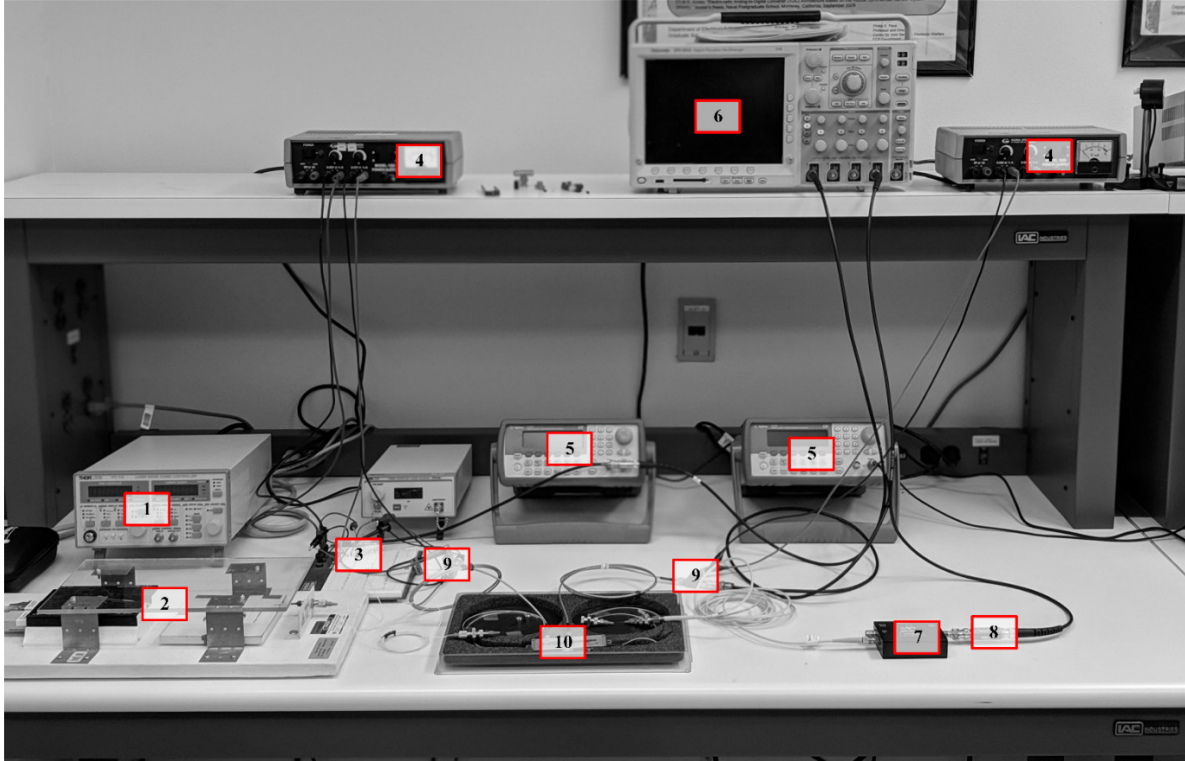


Figure 45. Optical Linearized Modulator Laboratory Setup

The linearized modulator is listed as having a combined insertion loss of 6.6 dB. A 93-mW laser source was sent through the modulator. The modulator bias levels were adjusted for maximum output intensity, and a combined insertion loss of 7.62 dB was recorded. The modulators capability to reproduce a pulse was first verified by connecting the pulse train and leaving RF2 unconnected. An optical pulse of  $\sim 200$  mV and  $\sim 30$ -ns wide was created, as shown in Figure 46. The square wave used as the multivibrator trigger input is shown in Figure 46a, and the optical linearized modulator output is shown in Figure 46b. There is an observable amount of optical noise at the output of the modulator. While relatively easy to filter out, this output does not represent the output after the interpolation filter, which integrates the optical noise into the output.

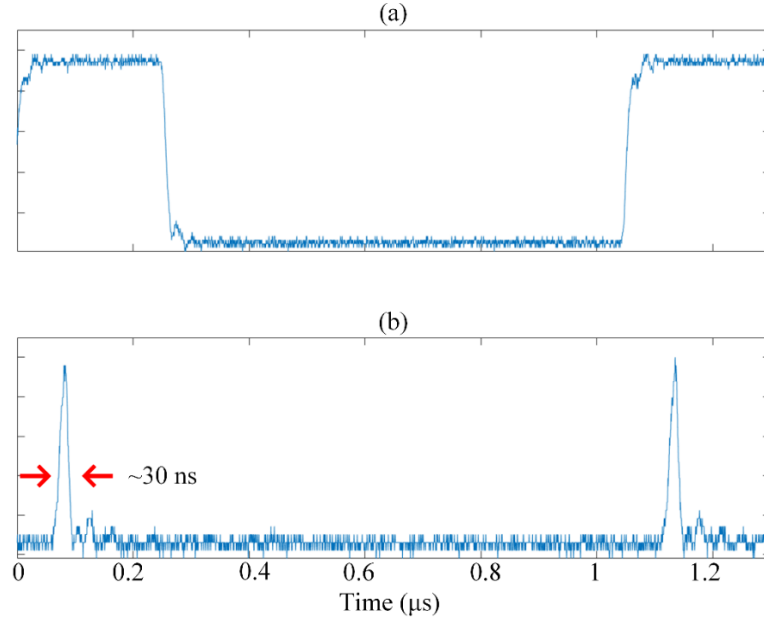


Figure 46. Optical Linearized Modulator Pulse

Next, the ability of the modulator to correctly undersample a signal placed on RF2 was tested. Accurate results from the linearized modulator were unable to be obtained. Upon close inspection, the modulator's two RF inputs appear to be jointly biased. This performance is insufficient for purposes in this research as the total modulator output is required to have zero optical intensity when there is no pulse at the input. The modulating wave placed on RF2 continually changed the bias level of the complete modulator. This is best shown in Figure 48; in this Figure, the output of the modulator is shown on channel 4 (green), the square wave used as the pulse trigger is shown on channel 1 (yellow), and the source placed on RF2 is shown on channel 3 (purple). As we see in Figure 47, the optical pulse is created with a width of 35 ns, but the modulator's output was never reduced to a level near zero intensity like in Figure 46 because of the constantly changing bias level produced by the source on RF2. This represents the output of the optical linearized modulator without the low-pass filter connected. While using the optical linearized modulator was a promising idea in reducing the amount of noise and power consumption in the photonic NYFR model, the modulator was unable to be configured correctly to undersample the RF input. Because of this, the cascade modulator was set aside for two separate modulators, which is described in the next section.



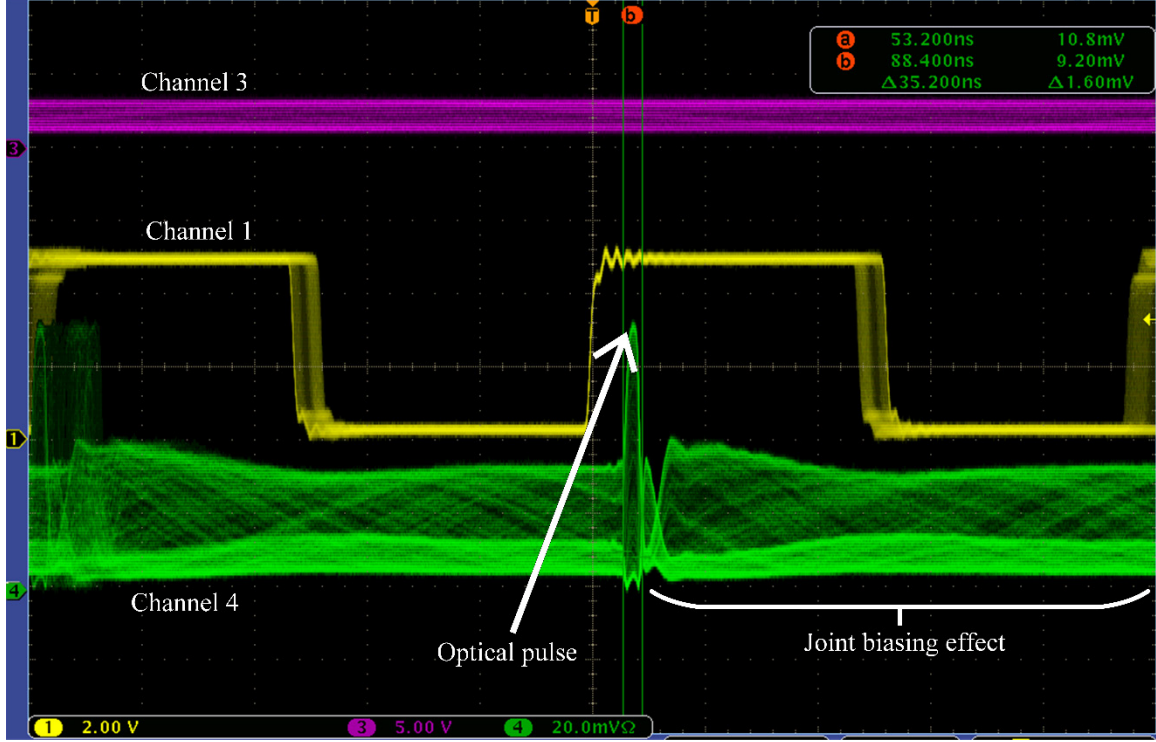


Figure 47. Optical Linearized Photonic NYFR Output

## B. DUAL MODULATOR NYFR TESTS

The design of the prototype photonic NYFR produced in [5] was modified to make improvements on the power management and increase the frequency range of identifiable input frequencies. The previous setup was used with the exception of replacing the optical linearized modulator with two JDSU X5 single drive modulators. The X5 has a separate input for driving the DC bias and a typical optical insertion loss of 4.5 dB. The laser source was used to test the combined optical insertion loss of the modulators and a loss of  $\sim 10$  dB was observed. The laboratory setup for the dual modulator tests is shown in Figure 48.

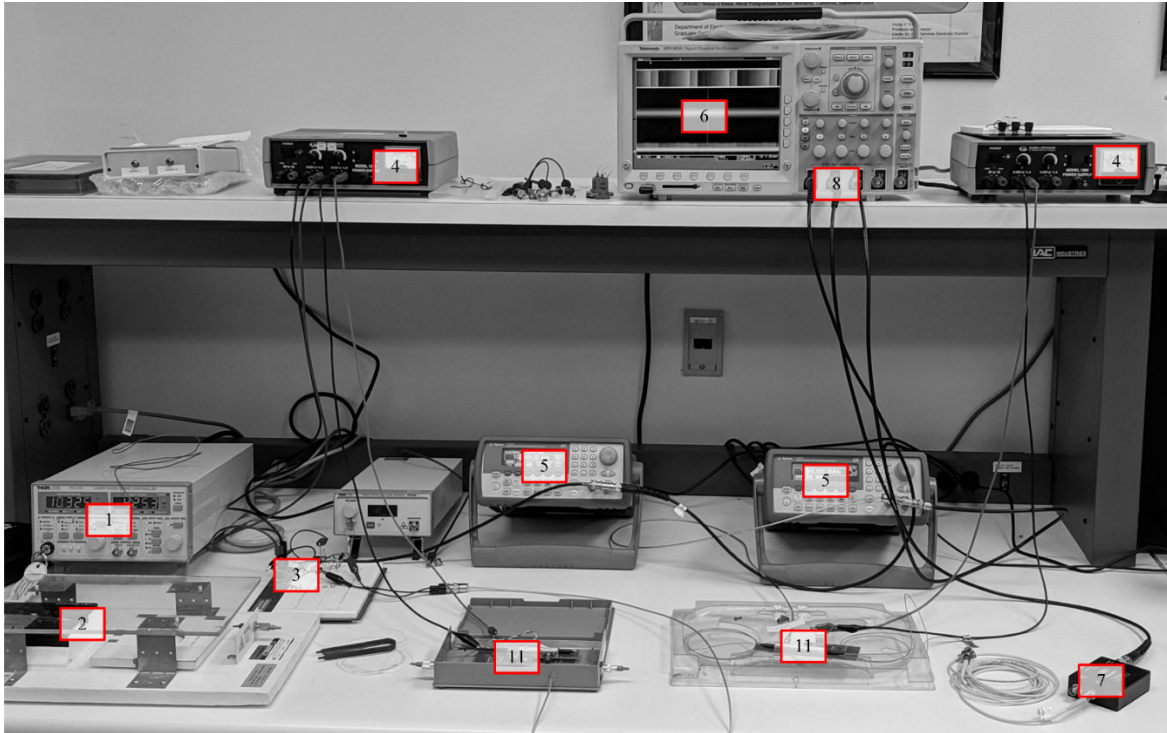


Figure 48. Dual Modulator Laboratory Setup

The ability of the dual modulators to correctly produce an optical pulse was tested first. The same pulse generation method as before was used and connected to the RF input of the first modulator; the output at the second modulator was recorded. A 36-ns pulse at  $\sim 30$  mV was successfully created; this result is shown in Figure 49. Channel one (yellow) is the square wave trigger for the optical pulses and channel four (green) is the resulting optical output from the second modulator. The next test determined the ability of the dual modulators to correctly undersample a signal placed on the second modulator. The result of a 500-kHz source placed on a pulse train with an average frequency of 1 MHz is shown in Figure 50; the optical intensity at the output of the modulator is observed to be varying in intensity as the source varies in voltage. Channel one (yellow) is the square wave trigger for the optical pulses, channel three (purple) is the modulating waveform placed on the second modulator for undersampling, and channel four (green) is the resulting optical pulses. A steady level of optical noise can be observed in the optical output. This test showed the successful undersampling of an RF input by the optical pulses.

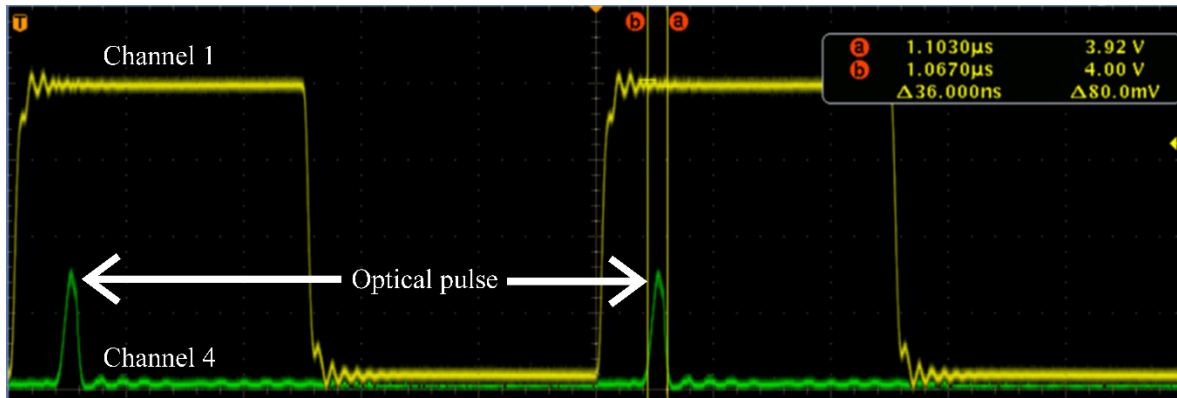


Figure 49. Dual Modulator Optical Pulses

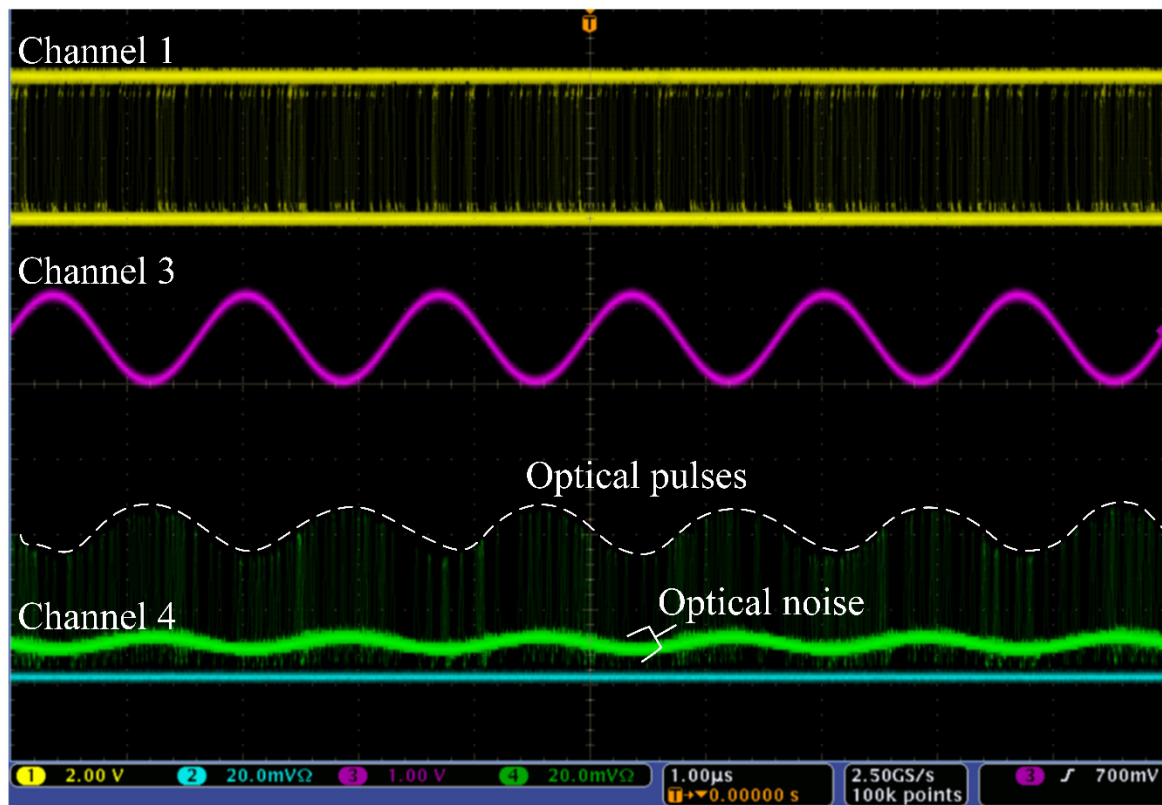


Figure 50. Dual Modulator Undersampling

The NYFR relies on an interpolation filter to sample at a rate independent of the phase modulation of the sampling waveform. A significant loss in voltage was observed when the output of the modulator was connected to the interpolation filter. The peak-to-peak amplitude of the output was reduced from  $\sim 30$  mV to less than 5 mV. This brought

the level of the output signal very close to the level of optical noise in the receiver model. The receiver was initially designed to use an average sampling pulse frequency of 1 MHz, but useful data was unable to be obtained using the 500-kHz low-pass filter with that frequency. The average sampling frequency of the sampling pulse was lowered to match the level of the low-pass filter. Because a function generator was used as a trigger for the pulse train, the phase modulation waveform takes the shape of a ramp. The parameters of the sampling pulse and ADC frequency are listed in Table 9.

Table 9. Laboratory Test Sampling Pulse

Center Frequency $f_{s1}$	Sweep Bandwidth $f_{BW}$	Sweep Frequency $f_{ST}$	Interpolation Filter $f_{INT}$	ADC Frequency $f_{ADC}$
500 kHz	100 kHz	50 Hz	500 kHz	1 MHz

Tests were conducted with varying input frequencies, but the result for the test using a 200-kHz source on the second modulator best describes the results received using this photonic NYFR model. At this frequency, the photonic NYFR with a pulse train and ADC rate as listed in Table 9 is not actually undersampling the input waveform. Because the photonic NYFR is sampling this signal above its Nyquist rate, the information recovery should not require the use of its compressed sensing model. The spectrogram of the square wave used as the trigger for the pulse train is shown side by side with the spectrogram of the output of the NYFR in Figure 51. The pulse train is folded back into the baseband when its frequency exceeds 500 kHz because of aliasing. What cannot be seen in this spectrogram is the affect the DC bias has on the output wave form. In Figure 52, the normalized frequency response of the NYFR is shown with and without the DC bias filtered. In Figure 52b, the source frequency is recovered in addition to other spurious frequencies. The effect of the optical noise can also be seen. Optical sampling pulses were successfully created using this photonic NYFR design and showed the successful undersampling of the input waveform prior to the interpolation filter but were unsuccessful in performing information recovery.

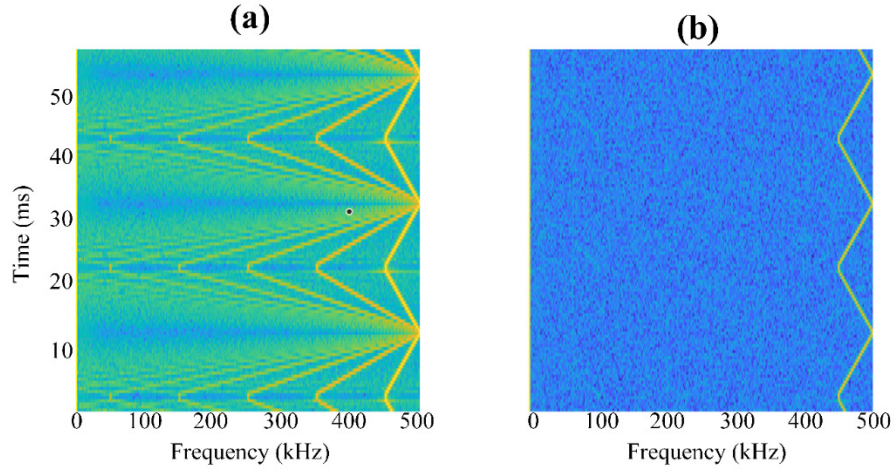


Figure 51. Photonic NYFR Spectrogram

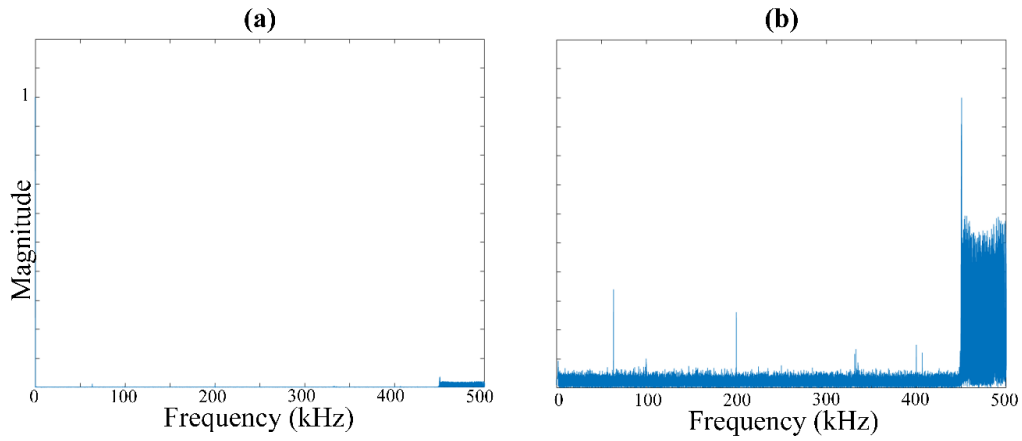


Figure 52. Photonic NYFR Normalized Frequency Response

### C. DUAL MODULATOR WITH AMPLIFIER NYFR TESTS

In order to overcome the low optical power at the photodiode, an RF amplifier was placed at the output of the photodiode. With this, the peak-to-peak NYFR output at the low-pass filter was increased to 100 mV. The laboratory setup is shown in Figure 53.



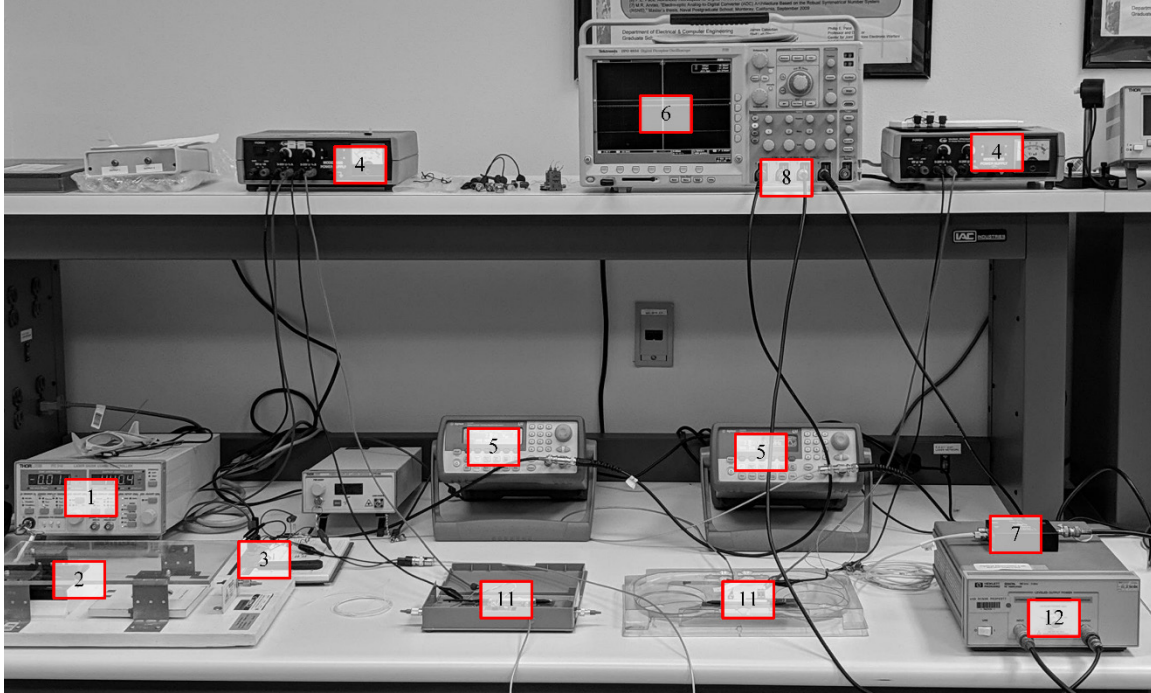


Figure 53. Dual Modulator with Amplifier Laboratory Setup

To observe the performance of the optical pulse train, the same parameters in Table 9 were used, but the sweep frequency was changed to 100 Hz and the ADC frequency to 5 MHz to observe the entire pulse train. The amplifier provided a better capture of the optical pulse train but it also added a noticeably greater source of noise in the frequency spectrum as it provides an increased bias and amplifies the optical noise. The output of the NYFR with the amplifier and its spectrogram are shown in Figure 54. In Figure 54a, channel one (yellow) is the square wave input to the pulse trigger, channel two (blue) is the output of the NYFR with interpolation filter and amplifier. In Figure 54b, the spectrogram of the NYFR output shows a noticeable increase in noise.

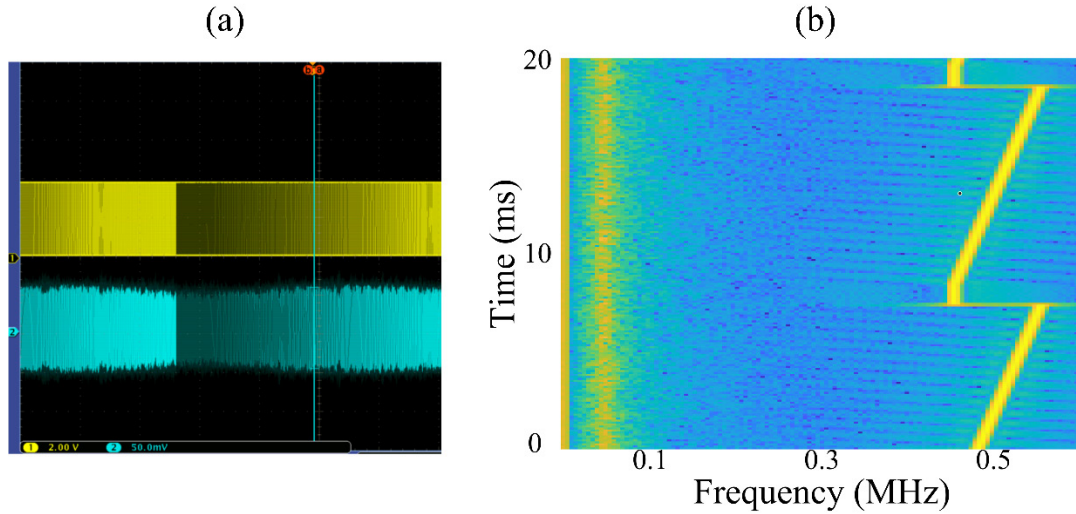


Figure 54. Photonic NYFR with Amplifier Pulse Train

The next test determined the ability of the photonic NYFR to recover signal information when the sampling pulses were at the Nyquist rate. A 100-kHz source was used as the input to the NYFR and an ADC rate of 1 MS/s. The signal information was recovered with a much greater degree of clarity. The spectrogram and frequency response of this test are shown in Figure 55.

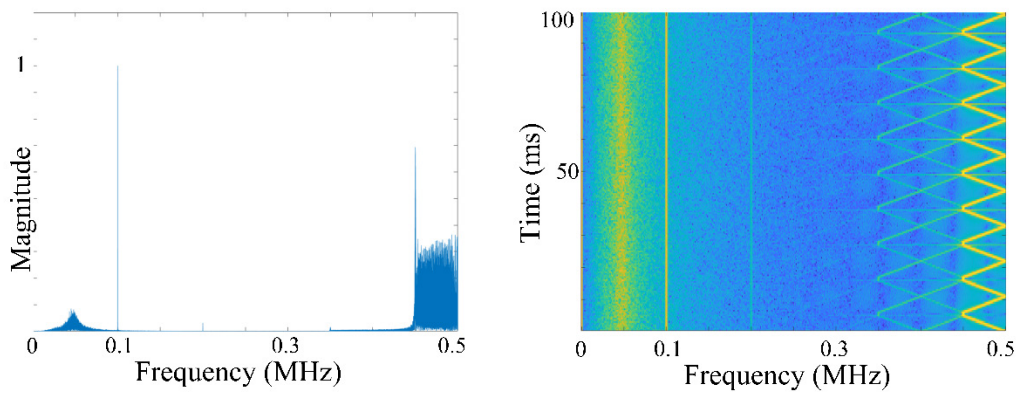


Figure 55. Photonic NYFR with Amplifier Nyquist Rate Results

Next, the ability of the photonic NYFR to recover a signal below the Nyquist rate was tested. A 750-kHz source was used as the input for the photonic NYFR and an ADC

of 1 MS/s was used to sample the output. The results were not as expected, but the signal information was able to be correctly recovered by using the visual method presented in (13). In addition to the optical and bias noise, a harmonic of the pulse train can be seen at a lower frequency. This may have been due to the reduction in pulse train frequency required of the prototype receiver to accommodate for the unexpected loss in power while attached to the low-pass filter. The results of this test are shown in Figure 56. The slope of the signal is highlighted by the red box and is equal to  $-10$ , the pulse train slope is  $10$ , and the center frequency of the NYFR output is 250 kHz.

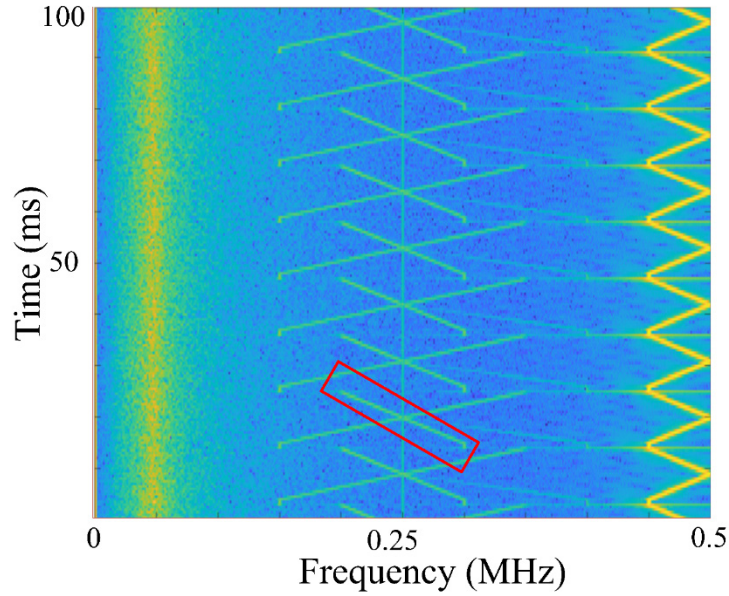


Figure 56. Photonic NYFR with Amplifier Undersampled Results #1

Higher input frequencies were used to test the ability of the photonic NYFR model to recover frequencies in higher Nyquist zones. The identification of the signal information became more difficult as the input frequency rate increased. A 2.05-MHz source was used as the input for the photonic NYFR, and an ADC of 1 MS/s was used to sample the output. This signal correlates to a signal in the  $-9$ th Nyquist zone, which is located in the 5th harmonic of the sampling pulse. The frequency information was unable to be recovered using the visual method. This is related to the width of the pulse train used, but the results



shown in Figure 57 are representation of how the spectrum of the photonic NYFR is impacted in a very sparse signal environment by noise produced in the receiver.

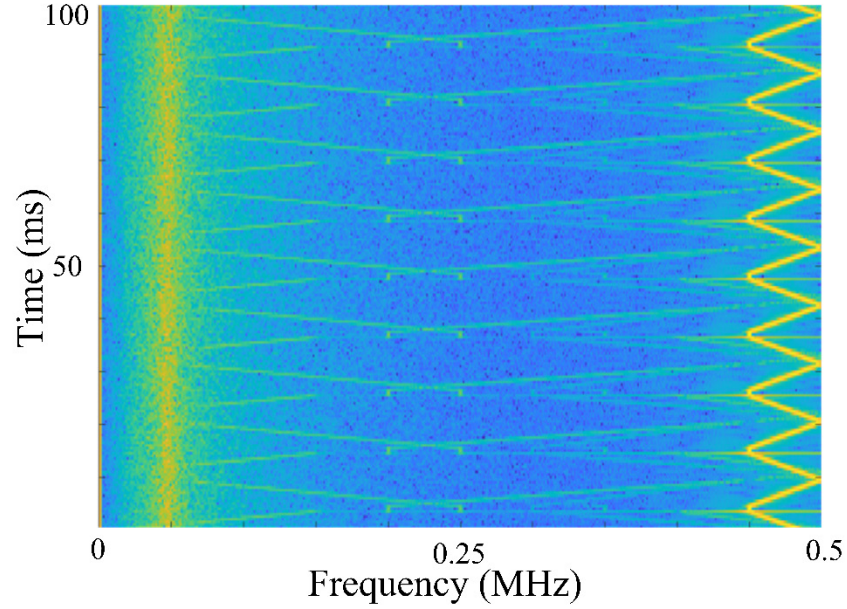


Figure 57. Photonic NYFR with Amplifier Undersampled Results #2

In this chapter, the design of three prototype NYFRs using commercial-off-the-shelf equipment was discussed. The design produced by Shmel in [5] was improved, a higher power laser source was used, an optical linearized modulator was tested, and an RF amplifier was added.

THIS PAGE INTENTIONALLY LEFT BLANK.

## **VI. CONCLUSIONS AND RECOMMENDATIONS**

Through software simulation, hardware simulation, and tests run in the laboratory, some of the functionality in using photonics in analog-to-information receivers was shown. The results were not as promising as expected, but there were lessons learned that may aid in future research on this topic.

### **A. CONCLUSIONS**

The objective of this research was to recover undersampled signal information using photonics and compressive sensing techniques. This signal information recovery using the OptSim software package was achieved but not with the hardware experimentation. OptSim provided for an extraordinary amount of control in the photonic components. A pulse of less than 1 ns was created, the ability to properly manage both the RF and optical power in the receiver was provided, and a wide variety of optical components to choose from were available. In the laboratory, the equipment available was limited, giving less control over the receiver parameters.

The photonic receiving models created required the use of DC bias voltage in several instances. This DC bias induced unwanted noise into the receiver output. In the laboratory experiment, the use of an RF amplifier was required to increase the power at the output of the photodiode to pass through the low-pass filter; this added additional noise to the output of the receiver.

While conducting tests with photonics in the use of the asynchronous multi-rate receiver, a conclusion was inferred that using photonics to sample RF signals provided no discernable benefit and only added to the level of difficulty in reconstructing the original signals. The NYFR is promising in this area because the interpolation filter eliminates the need for ADC synchronization. When precise samples are required, using RF components may be the best and most easily implemented solution.

This area of study warrants future research, but the benefit of using photonics as analog-to-information receivers may not be seen until the output is analyzed in the optical domain. Using the modulators as a sampling device and then a photodiode to bring the

undersampled signal back to the RF domain for analysis adds an unneeded step and noise to the output of the receiver.

## **B. FUTURE WORK**

Through experimentation, observation, and lessons learned, several areas have been identified in this thesis that may prove productive given future research.

### **1. Analyzing the Output in the Optical Domain**

Modulating the RF onto optical pulses and then converting the optical pulses back into the RF domain adds an unneeded step in the receiver model. In several discussions attempting to reduce complexity in the receiver models, we concluded that the benefit to the use of photonics may only be seen when the system is entirely photonic. Analyzing the receiver outputs in the optical domain may prove beneficial. This should be conducted in concert with traditional receivers using electrical components to compare the results.

### **2. Improve the Prototype Build**

The prototype NYFR has a large amount of room for improvement. While testing the prototype, a noticeable change in optical power was made simply by adjusting the placement of the fiber optic cables. A prototype model built with cables of precise length and constant position would benefit from a decreased loss in optical power.

Several different types of optical modulators may prove to be more useful in creating the optical pulses or modulating the RF onto the laser. Methods of increasing the optical power of the signal prior to the conversion back to electrical current may decrease the DC bias seen by the model.

The MZIs used in this research required an amount of bias tuning not tenable in a system intended for repeated or extended use. The MZIs have photodiodes embedded in their circuitry; experimentation in connecting the MZIs to a microcontroller or field-programmable gate array (FPGA) to automatically control the bias voltage should be conducted.

The method of pulse generation is not suitable for use at frequencies where A-to-I receivers are useful. The pulse created in the prototype build was 30 ns; this limits the ability to recover an undersampled signal to no greater than 30 MHz. Creating smaller, more uniform pulses aids in the recovery of signal information.

Finally, the output of the photonic A-to-I receiver, whether in the photonic or RF domain, may benefit from a connection to an FPGA to aid in the automated recovery of compressed signal information. The FPGA could provide multiple undersampling methods able to be used by the receiver, making this a multi-mode photonic A-to-I receiver.

THIS PAGE INTENTIONALLY LEFT BLANK.

## LIST OF REFERENCES

- [1] D. Reinsel, J. Gantz, J. Rydning, “The digitization of the world from edge to core,” IDC, Framingham, MA, USA, #US44413318, 2018. [Online]. Available: <https://www.seagate.com/files/www-content/our-story/trends/files/idc-seagate-dataage-whitepaper.pdf>
- [2] Federal Communications Commission, “Auction of 28 GHz upper microwave flexible use service licenses for next-generation wireless services closes,” public notice, Federal Communications Commission, Washington, DC, USA, 2018. [Online]. Available: <https://docs.fcc.gov/public/attachments/DA-19-23A1.pdf>
- [3] G. Fudge, R. Bland, M. Chivers, S. Ravindran, J. Haupt, P. E. Pace, “A Nyquist Folding Analog-to-Information Receiver,” in *Signals, Systems and Computers, 42nd Asilomar Conf.*, 2008. [Online]. doi: 10.1109/ACSSC.2008.5074464
- [4] R. Maleh, G. Fudge, F. Boyle, P. E. Pace, “Analog-to-Information and the Nyquist Folding Receiver,” *IEEE Journal on Emerging and Selected Topics in Circuits and Systems*, vol. 2, no. 3, pp. 564–578, September 2012. [Online]. doi: 10.1109/JETCAS.2012.2223611
- [5] R. Shmel, “Photonic compressed sensing Nyquist folding receiver,” M.S. thesis, Dept. of ECE., NPS, Monterey, CA, USA, 2017.
- [6] N. Tzou, D. Bhatta, B. Muldrey, T. Moon, X. Wang, H. Choi, A. Chatterjee, “Low cost sparse multiband signal characterization using asynchronous multi-rate sampling: Algorithms and Hardware.” *Jour. of Electronic Testing*, vol. 31, pp. 85–98, January 2015. [Online]. doi: 10.1007/s10836-015-5505-9
- [7] C. Shannon, “Communication in the presence of noise,” *Proceedings of the IEEE*, vol. 86, no. 2, pp. 447–457, 1998.
- [8] A. Oppenheim, A. Willsky, S. Nawab, *Signals and Systems*, 2nd ed. Upper Saddle River, NJ, USA: Prentice Hall, 1997.
- [9] D. Healy and D. Brady, “Compression at the physical interface,” *IEEE Signal Processing Magazine*, pp. 67–71, March 2008.
- [10] Maxim Integrated. “Jitter calculator,” 2019. [Online]. Available: <https://www.maximintegrated.com/en/design/tools/calculators/general-engineering/jitter.cfm>
- [11] A. Mishra and R. Verster, *Compressive Sensing Based Algorithms for Electronic Defence*. Cham, Switzerland: Springer, 2017

- [12] P. Ghelfi, F. Laghezza, F. Scotti, G. Serafino, A. Capria, S. Pinna, D. Onori, et al., “A fully photonics-based coherent radar system.” *Nature*, vol 507, pp. 341–345, March 2014. [Online]. doi: 10.1038/nature13078
- [13] Synopsys, Inc. *OptSim Models Reference Volume I Sample Mode*. Ossining, NY, USA, 2017.
- [14] P. E. Pace, A. Kusmanoff, G. Fudge, “Nyquist Folding Analog-to-Information Receiver: Autonomous information recovery using quadrature mirror filtering,” in *Conference Record of the Forty-Third Asilomar Conference on Signals, Systems, and Computers*, 2009. [Online]. doi: 10.1109/ACSSC.2009.5470156
- [15] E. van den Berg and M. Friedlander, “Probing the Pareto Frontier for basis pursuit solutions.” *SIAM Journal on Scientific Computing*, vol. 31, no. 2, pp. 890–912. [Online]. doi: 10.1137/080714488



## **INITIAL DISTRIBUTION LIST**

1. Defense Technical Information Center  
Ft. Belvoir, Virginia
2. Dudley Knox Library  
Naval Postgraduate School  
Monterey, California